PAUL SCHERRER INSTITUT

ETH
Eidgenössische Technische Hochschule Zürich
Swiss Federal Institute of Technology Zurich

Master Thesis

Double Degrader for Proton Therapy

Author:
Helene Stachel

Supervisors:
Dr. Andreas Adelmann
Prof. Klaus Kirch

Abstract

A double degrader setup was simulated with `OPAL` to test on a decrease in beam emittance. Instead of one conventional degrader, two thinner degraders with additional focusing elements are used to build a double degrader. The main idea is to refocus the beam after the first degradation such that the protons enter the second degrader with optimal alignment. The double degrader is designed for the medical purposes of proton therapy, where the proton beam delivered by the COMET cyclotron is taken into account. A degradation from a kinetic energy of 250 MeV to 72 MeV for protons travelling through a graphite double degrader setup (density $\rho = 1.88\ \mathrm{g/cm^3}$) leads to a reduction in beam emittance about a factor 1.40 when compared to a conventional degrader.

July 31, 2013

Contents

Helene Stachel
stachelh@phys.ethz.ch

Helene Stachel
stachelh@phys.ethz.ch

1. Motivation

Proton therapy is an efficient and precise way to destroy cancer cells without affecting much of the surrounding healthy tissue. The protons, previously accelerated by a cyclotron, enter the patients body and release most of its energy, obeying the scattering physics expressed in the Bethe-Bloch formula. Usually, the protons are accelerated with a cyclotron to a steady energy. Accordingly, these particles need to be slowed down to the specific energy of the patient needs. At PSI, the protons firstly become accelerated to a kinetic energy of 250 MeV by the cyclotron COMET. Subsequently, those protons need to be decelerated to 70 MeV for proton therapy. The element used to slow down protons is called a degrader. Nowadays, the degrader is a slab of material placed into the beamline, with shape and thickness adjusted to the amount of energy to be lost. This degrader mainly has two drawbacks

- energy spread,
- increase in phase space.

Protons entering the degrader undergo essentially multiple Coulomb scattering, single Rutherford scattering and inelastic scattering, which induces an angular spread. Furthermore, the amount of lost energy is not the same for every particle, but rather a probability distribution being approximately Gaussian. Hence, a beam passing through a degrader will experience an increase in phase space as well as a spread in energy. The necessary focusing elements, along with the supplementary energy selection system placed after such a degrader, are responsible for a considerable loss in beam intensity. The *double degrader* is a construct of two single degraders placed in series with some focusing elements in between. The additional focusing makes it possible to keep the beam size small and get access to a better control over the energy spread. Generally speaking, a beam sent through one degrader can only be focused on one point in or upon the degrader. For all remaining points, which the beam passes, travelling the degrader, the spread increases. Consequently, two single degraders placed in series, with additional focusing elements in between them, can be interpreted as one single degrader with two focusing points. Theoretically, a beam passing such a construction can not experience such a tremendous increase in spatial distribution and energy spread, as a beam travelling a single degrader.

Dr. Farley has done research on double degraders [Far05] and even filed a patent on a double degrader setup [FAR03]. He has worked out some formalism describing one, respectively multiple degraders placed in series. His research resulted in a decrease in beam emittance of about a factor N^2, where N is the number of single degraders placed in series. [Far05] achieved this result by assuming an input beam with zero emittance and linear beam optics.
Based on [Far05], Dr. Pedroni has made promising calculations based on Monte Carlo models to estimate the effect of scattering in the degrader [Ped12a], [Ped12b]. He found advantages of a double degrader setup over a conventional setup. The aim of this master thesis is to study a double degrader system as done in [Ped12a], [Ped12b] with `OPAL`. I want to

- add realistic initial phase space conditions
- study the effect of a very small beam size at the entrance of the second degrader
- analyse important nuclear reactions of protons in the range of 70 MeV to 250 MeV.

2. Dr. Farley's formalism and research

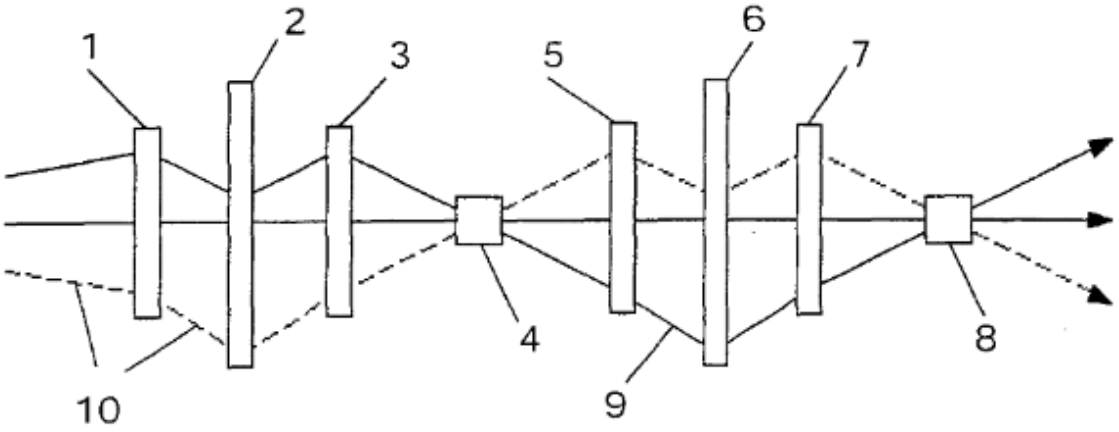

Figure 1: Francis J. M. Farley; Patent, International Publication Number WO 03/065382 A1

[Far05] proposes the usage of multiple degraders, as seen in figure 1. Labelled with number 4 and 8 are two slabs of materials called single degraders, which are placed in series with three focusing quadrupoles (labelled 5, 6 and 7) in between them. Dividing one degrader into several separate slabs and placing them in this way, decreases the beam emittance as the transversal spread is reduced [FAR03]. In the following section, the theoretical description of a beam passage through matter is discussed (following closely [Far05]).

2.1. Linear beam optics

In linear beam dynamics, the propagation of a particle can be described with $\mathbf{x}_2 = R \cdot \mathbf{x}_1$, where $R \in \mathbb{R}^{6\times 6}$ and $\mathbf{x}_1$, $\mathbf{x}_2$ are six-dimensional vectors $\mathbf{x}_{1,2}^{\mathrm{T}} = (x_{1,2}, \dot{x}_{1,2}, y_{1,2}, \dot{y}_{1,2}, z_{1,2}, \dot{z}_{1,2})$. The R - matrix is a transport matrix between point 1 and 2. Whenever the coupling between the horizontal and vertical plane is absent, one can reduce the six-dimensional R - matrix to a six-dimensional block matrix of the form

$$R = \begin{pmatrix} \begin{pmatrix} R_{11} & R_{12} \\ R_{21} & R_{22} \end{pmatrix} & 0 & 0 \\ 0 & \begin{pmatrix} R_{33} & R_{34} \\ R_{43} & R_{44} \end{pmatrix} & 0 \\ 0 & 0 & \begin{pmatrix} R_{55} & R_{56} \\ R_{65} & R_{66} \end{pmatrix} \end{pmatrix}. \tag{1}$$

Hence, it is possible to look at the equations for each plane separately

$$\begin{pmatrix} x_2 \\ \dot{x}_2 \end{pmatrix} = \begin{pmatrix} R_{11} & R_{12} \\ R_{21} & R_{22} \end{pmatrix} \begin{pmatrix} x_1 \\ \dot{x}_1 \end{pmatrix} = R \cdot \begin{pmatrix} x_1 \\ \dot{x}_1 \end{pmatrix}.$$

The same is valid for the y - and z - plane. In linear optics, the beam profile in one plane is described by an ellipse given with

$$\sigma^x = \begin{pmatrix} \sigma_{11} & \sigma_{12} \\ \sigma_{21} & \sigma_{22} \end{pmatrix}, \ \sigma^y = \begin{pmatrix} \sigma_{31} & \sigma_{32} \\ \sigma_{41} & \sigma_{42} \end{pmatrix}. \tag{2}$$

Applying the transport matrix to the phase space vector not only transforms the momenta and coordinates of each particle of a beam, but also the phase space ellipse to

$$\sigma_2^x = R^x \sigma_1^x \left(R^x\right)^T \text{ respectively } \sigma_2^y = R^y \sigma_1^y \left(R^y\right)^T. \tag{3}$$

2.1.1. Scattering action

Assuming no scattering takes place and the beam travels through vacuum only, then

$$R = \begin{pmatrix} 1 & L \\ 0 & 1 \end{pmatrix} \qquad (v << c)\,, \tag{4}$$

where L = length of the drift space the beam passes. According to equation 3, the phase space ellipse transforms as follows:

$$\sigma_2 = \begin{pmatrix} 1 & L \\ 0 & 1 \end{pmatrix} \cdot \begin{pmatrix} \sigma_{11} & \sigma_{12} \\ \sigma_{21} & \sigma_{22} \end{pmatrix} \cdot \begin{pmatrix} 1 & 0 \\ L & 1 \end{pmatrix} \tag{5}$$

$$= \begin{pmatrix} \sigma_{11} + 2L\sigma_{12} + L^2\sigma_{22} & \sigma_{12} + L\sigma_{22} \\ \sigma_{12} + L\sigma_{22} & \sigma_{22} \end{pmatrix}. \tag{6}$$

For small values of L the L^2-terms vanish and the derivative of the matrix σ, without scattering action, is

$$\frac{\mathrm{d}\sigma}{\mathrm{d}L} = \begin{pmatrix} 2\sigma_{12} & \sigma_{22} \\ \sigma_{22} & 0 \end{pmatrix}. \tag{7}$$

Hence the change in sigma by drift does not affect the term σ_{22}. To get the transfer map for particles traversing matter, a scattering term must be included. For a thin slab the scattering can not change σ_{11} nor the centre of the momenta distribution σ_{12}. However, the variance in the momenta σ_{22} changes. Adding scattering to the change in the sigma matrix delivers an additional term

$$\frac{\mathrm{d}\sigma}{\mathrm{d}L} = \begin{pmatrix} 2\sigma_{12} & \sigma_{22} \\ \sigma_{22} & \frac{\mathbf{K}}{\mathbf{p^2\beta^2}} \end{pmatrix}. \tag{8}$$

The value $\frac{K}{p^2\beta^2}$ incorporates momentum p, the ratio of particle and light velocity $\beta = \frac{v}{c}$ and the constant K, given with

$$K = 200 \cdot \frac{Z^2}{X_0}, \tag{9}$$

with charge of the beam particle Z and radiation length X_0 [GAA+00]. As we are interested in thick degraders, equation 8 must be integrated from zero to length D, where D is the thickness of one degrader. The integration results in

$$\sigma^{\text{out}} = \sigma^{\text{drift}} + \sigma^{\text{degrader}} \tag{10}$$

where σ^{beam} is equal to equation 5 and $\sigma^{\text{degrader}} = \begin{pmatrix} A & B \\ B & C \end{pmatrix}$ incorporates the coefficients

$$C(D) = \int_0^D \frac{K}{p^2\beta^2}\ \mathrm{ds} \tag{11}$$

$$B(D) = \int_0^D C(s)\ \mathrm{ds} \tag{12}$$

$$A(D) = 2 \cdot \int_0^D B(s)\ \mathrm{ds}. \tag{13}$$

$$\tag{14}$$

The degrader matrix depends only on A, B and C, which again depend on material constants 9 and

the momentum as well as $\beta = \frac{v}{c}$. Hence the beam profile 2 of the incoming beam has no influence on the degrader matrix.

2.1.2. Matching condition

The emittance is the determinant of the phase space ellipse and the quantity we want to minimize

$$\begin{aligned}\left(\epsilon^{\text{out}}\right)^2 = \det\,\sigma^{\text{out}} &= \left(\epsilon^{\text{beam}}\right)^2 + \left(AC - B^2\right) \\ &\quad + \left(C\sigma_{11}^{\text{beam}} + A\sigma_{22}^{\text{beam}} - 2B\sigma_{12}^{\text{beam}}\right) \qquad (15)\\ &= \left(\epsilon^{\text{beam}}\right)^2 + \left(\epsilon^{\text{degrader}}\right)^2 \\ &\quad + \left(C\sigma_{11}^{\text{beam}} + A\sigma_{22}^{\text{beam}} - 2B\sigma_{12}^{\text{beam}}\right). \qquad (16)\end{aligned}$$

The first line on the right hand side of equation 15 is invariable. We are not able to alter either $\left(\epsilon^{\text{beam}}\right)^2$ nor $\left(AC - B^2\right)$ by applying focusing. However, the second line of this equation shows a term, where the variables from the degrader matrix and the beam matrix get mixed. This mixed terms depend on the shape of the input beam and are minimized, if

$$C\mathrm{d}\sigma_{11}^{\text{beam}} + A\mathrm{d}\sigma_{22}^{\text{beam}} - 2B\mathrm{d}\sigma_{12}^{\text{beam}} = 0. \qquad (17)$$

Additionally, fixing the emittance of the input beam requires $\epsilon^{\text{beam}} = \sqrt{|\sigma^{\text{beam}}|}$ to be constant, thus $\left(\epsilon^{\text{beam}}\right)^2 = \sigma_{11}^{\text{beam}}\sigma_{22}^{\text{beam}} - \left(\sigma_{12}^{\text{beam}}\right)^2$ is constant. As a result, the variation of $\left(\epsilon^{\text{beam}}\right)^2$ is zero

$$\begin{aligned}0 &= \frac{\partial\left|\sigma^{\text{beam}}\right|}{\partial\sigma_{11}^{\text{beam}}}\cdot\mathrm{d}\sigma_{11}^{\text{beam}} + \frac{\partial\left|\sigma^{\text{beam}}\right|}{\partial\sigma_{22}^{\text{beam}}}\cdot\mathrm{d}\sigma_{22}^{\text{beam}} + \frac{\partial\left|\sigma^{\text{beam}}\right|}{\partial\sigma_{12}^{\text{beam}}}\cdot\mathrm{d}\sigma_{12}^{\text{beam}} \qquad (18)\\ &= \sigma_{22}^{\text{beam}}\cdot\mathrm{d}\sigma_{11}^{\text{beam}} + \sigma_{11}^{\text{beam}}\cdot\mathrm{d}\sigma_{22}^{\text{beam}} + 2\cdot\sigma_{12}^{\text{beam}}\mathrm{d}\sigma_{12}. \qquad (19)\end{aligned}$$

Solving equation 18 for $\mathrm{d}\sigma_{12}$ and inserting this into equation 17 delivers

$$\begin{aligned}0 &= C\mathrm{d}\sigma_{11}^{\text{beam}} + A\mathrm{d}\sigma_{22}^{\text{beam}} - 2B\mathrm{d}\sigma_{12}^{\text{beam}} \\ &= C\mathrm{d}\sigma_{11}^{\text{beam}} + A\mathrm{d}\sigma_{22}^{\text{beam}} - 2B\frac{\sigma_{22}^{\text{beam}}\cdot\mathrm{d}\sigma_{11}^{\text{beam}} + \sigma_{11}^{\text{beam}}\cdot\mathrm{d}\sigma_{22}^{\text{beam}}}{2\sigma_{12}^{\text{beam}}} \\ &= \left(C - B\cdot\frac{\sigma_{22}^{\text{beam}}}{\sigma_{12}^{\text{beam}}}\right) + \left(A - B\cdot\frac{\sigma_{11}^{\text{beam}}}{\sigma_{12}^{\text{beam}}}\right).\end{aligned}$$

This yields the matching condition $\frac{\sigma_{11}^{\text{beam}}}{\sigma_{12}^{\text{beam}}} = \frac{A}{B}$ and $\frac{\sigma_{22}^{\text{beam}}}{\sigma_{12}^{\text{beam}}} = \frac{C}{B}$, resulting in an optimal input beam with a shape

$$\begin{aligned}\sigma^{\text{beam}}_{\text{optimum}} &= \begin{pmatrix}\sigma^{\text{beam}}_{11} & \sigma^{\text{beam}}_{12}\\ \sigma^{\text{beam}}_{12} & \sigma^{\text{beam}}_{22}\end{pmatrix}\\ &= \begin{pmatrix}\frac{\sigma^{\text{beam}}_{12}}{B}\cdot A & \frac{\sigma^{\text{beam}}_{22}}{C}\cdot B\\ \frac{\sigma^{\text{beam}}_{11}}{A}\cdot B & \frac{\sigma^{\text{beam}}_{12}}{B}\cdot C\end{pmatrix}\\ &= \frac{\sigma^{\text{beam}}_{11}}{A}\cdot\begin{pmatrix}A & B\\ B & C\end{pmatrix}\\ &= \frac{\epsilon^{\text{beam}}}{\epsilon^{\text{degrader}}}\cdot\begin{pmatrix}A & B\\ B & C\end{pmatrix},\end{aligned} \tag{20}$$

where the relation $\frac{\sigma^{\text{beam}}_{11}}{A} = \frac{\sigma^{\text{beam}}_{12}}{B} = \frac{\sigma^{\text{beam}}_{22}}{C}$ was used as well as

$$\frac{\epsilon^{\text{beam}}}{\epsilon^{\text{degrader}}} = \sqrt{\frac{|\sigma^{\text{beam}}|}{AC-B^2}} = \sqrt{\frac{|\sigma^{\text{beam}}|}{A^2\cdot\frac{\sigma^{\text{beam}}_{22}\sigma^{\text{beam}}_{11}}{\left(\sigma^{\text{beam}}_{11}\right)^2}-\frac{\left(\sigma^{\text{beam}}_{12}\right)^2}{\left(\sigma^{\text{beam}}_{11}\right)^2}}} = \sqrt{\frac{\left(\sigma^{\text{beam}}_{11}\right)^2}{A^2}} = \frac{\sigma^{\text{beam}}_{11}}{A}. \tag{21}$$

Finally, inserting equation 20 into $\sigma^{\text{out}}_{\text{optimum}} = \sigma^{\text{beam}}_{\text{optimum}} + \sigma^{\text{degrader}}$

$$\sigma^{\text{out}}_{\text{optimum}} = \left(1+\frac{\epsilon^{\text{beam}}}{\epsilon^{\text{degrader}}}\right)\cdot\begin{pmatrix}A & B\\ B & C\end{pmatrix} \tag{22}$$

$$\begin{aligned}\rightarrow \epsilon^{\text{out}}_{\text{min}} &= \sqrt{\left|\sigma^{\text{out}}_{\text{optimum}}\right|}\\ &= \sqrt{\left(1+\frac{\epsilon^{\text{beam}}}{\epsilon^{\text{degrader}}}\right)^2\cdot\left(\epsilon^{\text{degrader}}\right)^2}\\ &= \epsilon^{\text{degrader}}+\epsilon^{\text{beam}}.\end{aligned} \tag{23}$$

As a result, the minimum output emittance is the superposition of two separate emittances, one arising from drift and the other from scattering inside the degrader material. Transferring this result for a beam interacting with one single degrader to a beam interacting with multiple degraders, gives rise to:

$$\begin{array}{lll}\text{1 degrader:} & \epsilon^{\text{out}}_{\text{min}} & = \epsilon^0+\epsilon^{\text{degrader}}\\ \text{N degraders:} & \epsilon^{\text{out}}_{\text{min}} & = \epsilon^0+\sum_{j=1}^{N}\epsilon^{\text{degrader}}_j\end{array}$$

Theoretically, such a minimum output emittance is possible, placing optical beam elements between the N degraders, shaping the beam in a manner, such that the matching conditions are fulfilled for each single degrader.
[Far05] claims that, for each degrader slab in each transversal plane, the loss in beam emittance is about a factor one. Hence, for each transversal plane, the beam emittance loss is about a factor N. In total, the beam emittance is decreased maximally by a factor N^2, compared to the best emittance achievable with a single degrader.

3. Previous research on double degader

Farley's promising increase in intensity led to Dr. Eros Pedroni do further research on this topic, which itself again delivered promising results. In addition to Pedroni's work, Dr. Christian Baumgarten did research on a double degrader.

3.1. Dr. Eros Pedroni's research

Pedroni did simulations with TRIM 2011, a simple Monte Carlo code [Zie13], to verify or dismiss Farley's concepts [Ped12b]. Firstly, the passage of a beam of protons through a slab of carbon ($\rho = 2.26$ g/cm^3) with a thickness of 167 mm and an input energy of 250 MeV is simulated. This single degrader slows the protons down to an energy of 70 MeV. Secondly, the passage of protons through two, three or four degraders was simulated, whereat these degraders were designed in a way such that the protons once more slowed down from a kinetic energy of 250 MeV to 70 MeV. By doing those simulations, in [Ped12b] is assumed

- linear beam optics and idealized refocusing (mirror imaging and time reversal),
- slab material is carbon ($\rho = 2.26 \frac{\text{g}}{\text{cm}^3}$),
- input beam consists of protons and has zero emittance,
- the protons become decelerated from an energy of 250 MeV down to 70 MeV,
- no chromatic effects,
- additional energy loss of about $\sim$ 30% due to nuclear interactions, which are not treated in TRIM.

The results of those simulations are listed in table 1. One now could argue against a double degrader, because it is possible to achieve better results with a triple or a quadruple degrader. However, the usage of a triple or even a quadruple degrader is ruled out by the design of the beam injection [Ped12b]. The more material slabs are placed in series, the thinner each slab becomes, the smaller the output emittance. Pedroni assumed zero input emittance, arguing that a realistic input emittance is of order $\epsilon \approx 5$ mm mrad, which is a factor 10 smaller than the output emittance of a single degrader. Consequently, as long as the input emittance is negligible compared to the output emittance, it can be set to zero. Using many degrader units gives rise to an output emittance comparable to the input emittance, which disregards the assumption of zero input emittance. As a result, the beam injection limits the number of degrader units to use. For this reason, we restrict ourselves to 2 degrader units. For the case of a double degrader, the two transversal planes experience a decrease in emittance of about a factor 1.85 each, respectively a factor $\approx \mathbf{3.48}$ in total [Ped12b].

Number of degraders	Emittance [mm mrad]
1	15.7
2	8.5
3	6.3
4	4.1

Table 1: Results of a Monte Carlo simulation with protons decelerated from 250 MeV to 70 MeV. These numbers are valid only for one transverse direction. The gain in phase space goes in quadrature, when considering both transverse planes.

3.2. Dr. Christian Baumgarten's research

Dr. Christian Baumgarten tackled the problem from another point of view as Pedroni, to verify or dismiss the possibility of an increase in beam intensity, specifically for gantry 3 at PSI [Bau13]. He performed a 4th-order Runge-Kutta integration to calculate the degrader matrix shown in equation 20, verifying [Far05]. Applying more realistic boundary conditions with regard to gantry 3 at PSI, in [Bau13] is assumed

- linear beam optics,
- input beam has zero emittance and 250 MeV,
- no chromatic effects,
- slab material is graphite $\left(\rho = 2.265 \frac{\mathrm{g}}{\mathrm{cm}^3}\right)$,
- quadrupole triplet as a focusing element with realistic size and field boundaries.

Baumgarten used `TRANSPORT` to estimate the quadrupole triplet necessary to refocus the beam, after passing the first and before entering the second degrader unit. The disillusioning result is a superconducting quadrupole triplet, which does not suit the needs for a proton therapy center. Instead of testing an unrealistic quadrupole triplet with superconducting magnets, Baumgarten adjusts the length of the first material slab, such that the beam passing through it can be refocused using a standard quadrupole triplet. This trade-off allows only a degradation from 250 MeV to 235 MeV for the first degrader unit and needs a degradation from 235 MeV to 70 MeV by the second degrader unit. This setup delivers in best case a reduction in emittance of $\approx 13\%$, hence a gain in intensity by a factor $\approx \mathbf{1.32}$.

3.3. Aim of this master thesis

This master thesis supplements the work done by Farley, Pedroni and Baumgarten. Simulations will be done using `OPAL` ([AAC+13], [Ade13]), similarly to Pedroni's simulations with `TRIM`. The main difference to Pedroni's simulations are more realistic boundary conditions. Contrarily to [Bau13], the simulations presented here are not restricted to the focusing elements used at PSI. The boundary conditions assumed here are

- linear beam optics,
- no chromatic effects,
- input beam emittance is not zero,
- input beam energy is 250 MeV,
- slab material is graphite $\left(\rho = 1.88 \frac{\mathrm{g}}{\mathrm{cm}^3}\right)$.

4. Passage of charged particles through matter in OPAL

OPAL (**O**bject Oriented **P**arallel **A**ccelerator **L**ibrary) is a tool to simulate the passage of charged particles through accelerator structures [AAC+13]. It has two big advantages compared to common simulation programs

- OPAL performs the calculations parallel on multiple cores,
- OPAL can handle multiple concatenated accelerator elements.

Furthermore, OPAL has multiple materials and focusing elements ready to use. Hence, it should be a manageable task to write a model for a double degrader and test at first Farley's initial increase in beam intensity, assuming idealized conditions. Secondly, changing the idealized conditions to more realistic ones and varying the focusing elements comes into reach.

Before using OPAL to simulate even a single degrader, OPAL needs to be tested on reliability. In order to do so, a beam with 10^5 protons, at an energy of 72 MeV, travelling through a 9 cm long collimator, was not only simulated with OPAL, but also with FLUKA [FFR+11]. FLUKA is a Monte Carlo simulation package, capable to simulate the passage of charged particles through matter. Moreover, FLUKA incorporates more physical effects than OPAL. Unfortunately, FLUKA is limited in use for beam lines. Hence, in this thesis FLUKA is used solely to check on the passage of particles through matter for comparison. Considering the passage of protons through material, OPAL treats energy loss due to the Bethe-Bloch formula and multiple Coulomb as well as single Rutherford scattering. On top of this, FLUKA also incorporates inelastic scattering. As a conclusion, the results from FLUKA are more precise, but should deliver the same results as OPAL for the energy degradation of protons travelling through material without undergoing inelastic scattering. The contribution from the inelastic scattering are secondary protons leaving the degrader setup at a wider angular spread and with lower kinetic energies than the initial protons do.

For protons with an energy of 70 MeV, the scattering model in OPAL workes well. However, for energies between 120 MeV and 250 MeV, the simulations from OPAL show discrepancies when compared to FLUKA. Hence, it is necessary to adjust the scattering model in OPAL to the physics of protons at energies higher than 70 MeV. This makes it worth to have a closer look into the parts of the OPAL-library, which are connected to the passage of charged particles through matter. This section deals with the scattering physics implemented in OPAL and explains, where modifications were necessary.

4.1. Theoretical background of the passage of charged particles through matter

4.1.1. Energy loss

The energy loss is calculated in OPAL with the Bethe-Bloch formula [BAB+12]

$$-\left\langle \frac{\mathrm{dE}}{\mathrm{dx}} \right\rangle = Kz^2 \frac{Z}{A} \frac{1}{\beta^2} \cdot \left[\frac{1}{2} \ln \frac{2m_e}{I^2 c^2 \beta^2 \gamma^2 T_{\max}} - \beta^2 - \frac{\delta(\beta\gamma)}{2} \right], \tag{24}$$

with

Z	Atomic number of absorber	
A	Atomic mass of absorber	
z	Charge number of incident particle	
m_e	Electron mass	0.510998918 MeV/c^2
M	Incident particle mass	MeV/c^2
N_A	Avogadro's number	6.0221415×10^{23} mol^{-1}
$\frac{K}{A}$	$4\pi N_A r_e^2 m_e c^2/A$	0.307075 MeVcm^2/g
r_e	Classical electron radius	2.817940325 fm
I	Mean excitation energy	eV
c	Speed of light	0.299792458×10^9 m/s
$\delta(\beta\gamma)$	Density effect correction to ionization energy loss	≈ 0
$T_{\max}$	Maximum kinetic energy which can be imparted to a free electron in a single collision	eV

where

$$T_{\max} = \frac{2m_e c^2 \beta^2 \gamma^2}{1 + 2\gamma m_2/M + (m_e/M)^2} \tag{25}$$

is the maximum energy which can be transferred by an head-on collision [Leo94]. The density effect accounts for the electric field, arising from the moving incident particles (in our case protons). This field polarizes atoms along its path, which shields electrons far away from the particle's path. This reduces the scattering loss of the outer electrons and needs to be subtracted from the original Bethe-Bloch formula, which does not include the density effect. The density effect can be calculated using Sternheimer's parametrization and depends on the atomic number Z of the absorber, as well as on the incident particle's kinetic energy [Leo94]. However, the incident particle's kinetic energy treated in this thesis is maximally 250 MeV, for which the density effect still is negligible.

For thick absorbers, or in different words, for a sufficient number of collisions, the energy loss distribution approaches the Gaussian form

$$f(x, \Delta) \propto e^{-\frac{(\Delta - \bar{\Delta})^2}{2\sigma}} \tag{26}$$

where Δ is the energy loss in the absorber, $\bar{\Delta}$ the mean energy loss, σ the standard deviation and x the absorber's thickness. For nonrelativistic heavy particles, the sigma value was calculated to be [Leo94]

$$\sigma_0^2 = 4\pi N_A r_e^2 \left(m_e c^2\right)^2 \rho \frac{Z}{A} x, \tag{27}$$

where ρ is the target's density and x the target's length.

4.1.2. Scattering

A charged particle moving through a material is mainly deflected by multiple Coulomb scattering and rarely by large angle Rutherford scattering. Superposing those two scattering models, delivers the final angular distribution, calculated in `OPAL` and described in [Jac06, ch. 13.6]

$$P_{\text{multiple scattering}} = \frac{1}{\sqrt{\pi}} e^{-\alpha^2} \mathrm{d}\alpha \tag{28}$$

$$P_{\text{single scattering}} = \frac{1}{8 \log 204 Z^{-\frac{1}{3}}} \frac{\mathrm{d}\alpha}{\alpha^3} \tag{29}$$

with the relative, projected angle $\alpha = \frac{\theta}{\langle \Theta^2 \rangle^{\frac{1}{2}}}$.

J. D. Jackson treats the passage of charged particles through matter in the same way Bruno Rossi [Ros52, ch. 2] does. Most particles from a beam travelling through a slab of matter will only be deflected about a small angle. At some point, however, single scattering occurs, where the involved particle experiences a greater deflection. Hence, when looking at the angular particle distribution of a beam, leaving a slab of matter

- particles leaving under a small angle are highly likely to have undergone multiple Coulomb scattering.
- particles leaving under a large angle are likely to have undergone single Rutherford scattering.

Accordingly, at some transition point, the multiple Coulomb scattering becomes less dominant and single Rutherford scattering takes over. Jackson estimated the transition point from multiple Coulomb to single Rutherford scattering to be 2.5α. Previously to Jackson's work on this topic, Snyder and Scott published a paper concerning this issue. Their results are similar to Jackson's result and can be seen in figure 2.

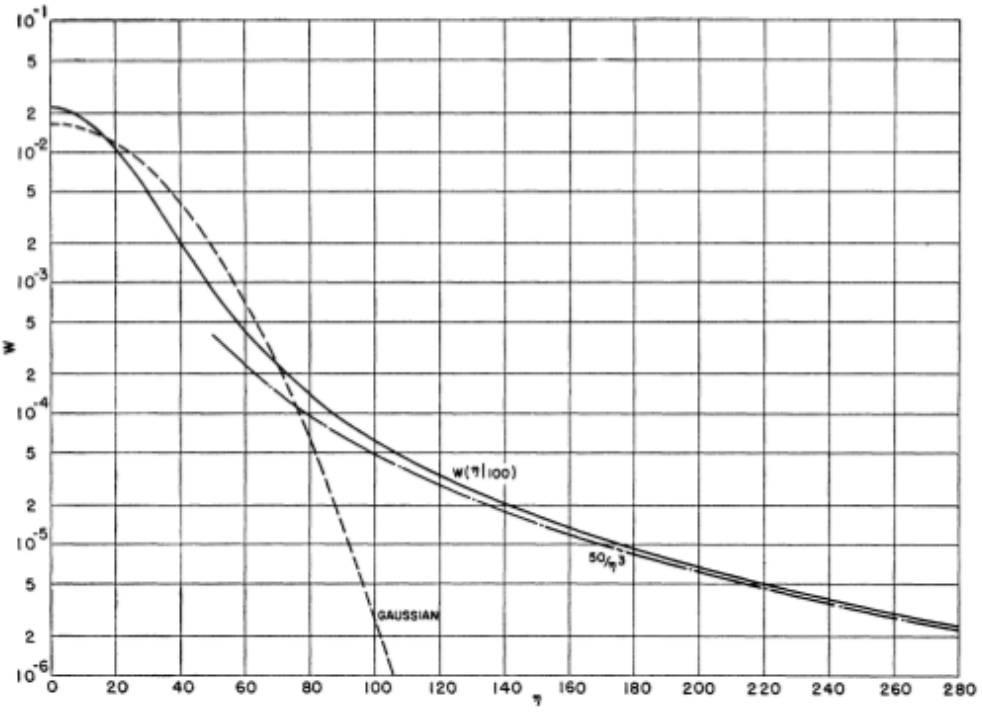

Figure 2: This plot is taken from [SS49]. The dashed line shows a Gaussian, which represents multiple Coulomb scattering. Snyder and Scott estimated an angular distribution function $W(\nu, z)$, incorporating both, multiple Coulomb and single Rutherford scattering. The average number of collisions a particle undergoes, travelling Snyder's and Scott's foil, is labelled z and ν is the angle about which the particle is deflected after z collisions. Scott and Snyder assumed the large angle Rutherford scattering to obey a distribution function $P_{\text{large angle}} \approx z/2\nu^3$, which is comparable to formula 29 for large ν. This plot shows the Gaussian for multiple Coulomb scattering, $P_{\text{large angle}} \approx z/2\nu^3$ for single Rutherford scattering and the combination of both in $W(\nu, z)$.

4.2. Model in OPAL

A partial implementation of the physics concerning the sections 4.1.1 and 4.1.2 in OPAL, was done by Yuanjie Bi in collaboration with Andreas Adelmann and Daniela Kiselev. My contribution to the scattering physics in OPAL is the rotation of the particle's reference system about θ_{plane} in combination with the rotation of the particle's trajectory about θ_{Coulomb} and $\theta_{\text{Rutherford}}$.

4.2.1. Implementation of Bethe-Bloch

OPAL tracks particles through an arrangement of elements. Tracking in this context means defining a step width Δt in time, respectively Δs in space, along the particles trajectory. Successively, for each step, the momenta and space coordinates are estimated for each particle, with respect to the boundary conditions, which the accelerator elements impose.
As soon as a particle hits a material, the particles energy loss is calculated using

$$-\left\langle \frac{\mathrm{dE}}{\mathrm{dx}} \right\rangle = K z^2 \frac{Z}{A} \frac{1}{\beta^2} \cdot \left[\frac{1}{2} \ln \frac{2 m_e}{I^2 c^2 \beta^2 \gamma^2 T_{max}} - \beta^2 \right] \tag{30}$$

with the variables described in section 4.1.1 and $T_{\max}$ from equation 25. Consequently, $-\left\langle \frac{\mathrm{dE}}{\mathrm{dx}} \right\rangle \cdot \Delta s \cdot \rho = \bar{\epsilon}$ delivers the energy a particle looses in average, travelling a material with density ρ, when looking at a single step with step width Δs. To accommodate the Gaussian approximation for thick absorbers, the actual energy loss the particles experiences is calculated by picking a random value from

$$f(\Delta s, \epsilon) = e^{-\frac{(\epsilon - \bar{\epsilon})^2}{2\sigma}} \tag{31}$$

with $\sigma = \sqrt{4\pi N_A r_e^2 \left(m_e c^2\right)^2 \rho \frac{Z}{A} \Delta s}$, using a random number generator.

4.2.2. Implementation of multiple Coulomb scattering

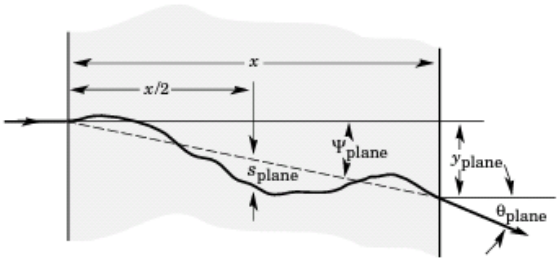

Figure 3: This figure is copied from the Physical Review [BAB+12, ch. 30.3] and shows the quantities used to describe multiple Coulomb scattering. The particle is incident in the plane of the figure. As we track each single particle step by step, the length x given in this figure corresponds to step width Δs used in the formulas in this section 4.2.2

This section summarizes chapter 30.3 from the Physical Review [BAB+12], which tells how multiple Coulomb scattering applies on charged particles traversing matter.
The notation used in the Physical Review is slightly different than the one from Jackson. Therefore, notations and formulas from both sources are brought together and connected to each other in this section.
Following Jackson [Jac06], described in section 4.1.2, the angular distribution for multiple Coulomb scattering is

$$P_{\text{multiple scattering}} = \frac{1}{\sqrt{\pi}} e^{-\alpha^2} \mathrm{d}\alpha \tag{32}$$

with the relative, projected angle $\alpha = \frac{\theta}{\langle \Theta^2 \rangle^{\frac{1}{2}}}$. In the Physical Review, the multiple scattering is treated in each plane independently. This requires a careful treatment of the projected angle

$$\theta_0 = \theta_{\text{plane}}^{\text{rms}} = \frac{1}{\sqrt{2}} \theta_{\text{space}}^{\text{rms}} \rightarrow \left\langle \Theta^2 \right\rangle^{\frac{1}{2}} = \sqrt{2} \cdot \theta_0. \tag{33}$$

The value for θ_0 was estimated by Gerald R. Lynch and Orin I. Dahl to be [LD91] [1]

$$\theta_0 = \frac{13.6 \text{ MeV}}{\beta cp} z \sqrt{\Delta s / X_0} \left[1 + 0.038 \ln \Delta s / X_0\right], \tag{34}$$

where X_0 is the radiation length of the target material. The deflections into the planes $\theta_{\text{plane},x}$ and $\theta_{\text{plane},y}$ are assumed to be independent and identically distributed. The quantities shown in figure 3 describing multiple Coulomb scattering then are

$$\psi_{\text{plane}}^{\text{rms}} = \frac{1}{\sqrt{3}} \theta_{\text{plane}}^{\text{rms}} = \frac{1}{\sqrt{3}} \theta_0, \tag{35}$$

$$y_{\text{plane}}^{\text{rms}} = \frac{1}{\sqrt{3}} \Delta s \cdot \theta_{\text{plane}}^{\text{rms}} = \frac{1}{\sqrt{3}} \theta_0 \Delta s \tag{36}$$

$$\text{and} \quad s_{\text{plane}}^{\text{rms}} = \frac{1}{4\sqrt{3}} \Delta s \cdot \theta_{\text{plane}}^{\text{rms}} = \frac{1}{4\sqrt{3}} \theta_0 \Delta s. \tag{37}$$

These equations are only valid for small $\theta_{\text{plane}}^{\text{rms}}$, thus ignoring large angle Rutherford scattering. To do a Monte Carlo simulation, to get the random but correlated values s, ψ, y and θ, the Physical Review suggests to work with two independent Gaussian random variables z_1 and z_2 and calculate

$$y_{\text{plane}} = \frac{z_1 \theta_0 \Delta s}{\sqrt{12}} + \frac{z_2 \theta_0 \Delta s}{2}, \tag{38}$$

$$\theta_{\text{plane},y} = z_2 \theta_0. \tag{39}$$

As we assumed the deflections to be independent and identically distributed, the values s, ψ, x and θ for the $\theta_{\text{plane},x}$ can be calculated with a Monte Carlo simulation in exactly the same way as for $\theta_{\text{plane},y}$.

4.2.3. Implementation of single Rutherford scattering

Every particle traversing a material experiences multiple Coulomb scattering. However, not so many particles experience single Rutherford scattering. The percentage of particles undergoing large angle scattering is

$$\chi_{\text{single}} = \frac{\int_{2.5}^{\infty} P_{\text{single scattering}}(\alpha)\, \mathrm{d}\alpha}{\int_0^{2.5} P_{\text{multiple scattering}}(\alpha)\, \mathrm{d}\alpha + \int_{2.5}^{\infty} P_{\text{single scattering}}(\alpha)\, \mathrm{d}\alpha} \tag{40}$$

$$= \frac{\int_{2.5}^{\infty} \frac{1}{8 \ln \frac{204}{Z^{1/3}}} \mathrm{d}\alpha}{\int_0^{2.5} \frac{1}{\sqrt{\pi}} e^{-\alpha^2} \mathrm{d}\alpha + \int_{2.5}^{\infty} \frac{1}{8 \ln \frac{204}{Z^{1/3}}} \mathrm{d}\alpha} \tag{41}$$

$$= \begin{cases} 0.00409517 & \text{Beryllium} & (Z = 4) \\ 0.00421168 & \text{Graphite} & (Z = 6) \\ 0.00473515 & \text{Copper} & (Z = 29) \\ 0.00487766 & \text{Molybdenum} & (Z = 42) \end{cases}. \tag{42}$$

In order to respect χ_{single}, a random number ξ_1 between 0 and 1 is picked. If and only if this random number is smaller than the percentage of particles undergoing large angle scattering, hence $\chi_{single} > \xi_1$, the particle undergoes single Rutherford scattering. The values for χ_{single} do not change much with different atomic numbers Z hence, a fix value $\chi_{\text{single}} = 0.0042$ is implemented in `OPAL`, to avoid unnecessary integrations and shorten the programs runtime.

[1] Be careful, there is an errata in this paper in formula (12) on page 10. However, the formula 33 used here is correct and can be looked up in the Physical Review [BAB+12].

To do single Rutherford scattering, a second random number ξ_2 between 0 and 1 is necessary to decide, which angle larger $2.5 \cdot \alpha$ is the angle, the particle rotates about. The third and last random number ξ_3 is needed to determine, whether the rotation is up- or downwards, respectively to give the rotation angle a positive or a negative sign:

$$\theta_{\text{Rutherford}} = \begin{cases} +2.5\sqrt{\frac{1}{\xi_2}} \cdot \theta_0, & \xi_3 > 0.5 \\ -2.5\sqrt{\frac{1}{\xi_2}} \cdot \theta_0, & \xi_3 < 0.5 \end{cases} \tag{43}$$

4.2.4. Rotation of the reference system

In every time step, as long as a particle is inside a material, `OPAL` repeats subsequently the following steps

i calculate the loss in energy,

ii delete the particle if the particle's kinetic energy is smaller than 0.1 MeV,

iii apply Coulomb scattering,

iv rotate the reference system of the particle accordingly,

v pick a random number χ_1 and do Rutherford scattering if $\chi_1 > \xi_1$ as well as a rotation of the particle's reference system.

Every time a particle rotates about θ_{Coulomb} or $\theta_{\text{Rutherford}}$, the reference system must be adjusted to the new direction of movement. In section 4.2.2 and 4.2.3, the scattering angle is calculated with regard to the particle's direction of movement as drawn in figure 3. To re-align the particle's direction of movement with this axis, the particle's reference system must be rotated about $\psi_{x,z}$.

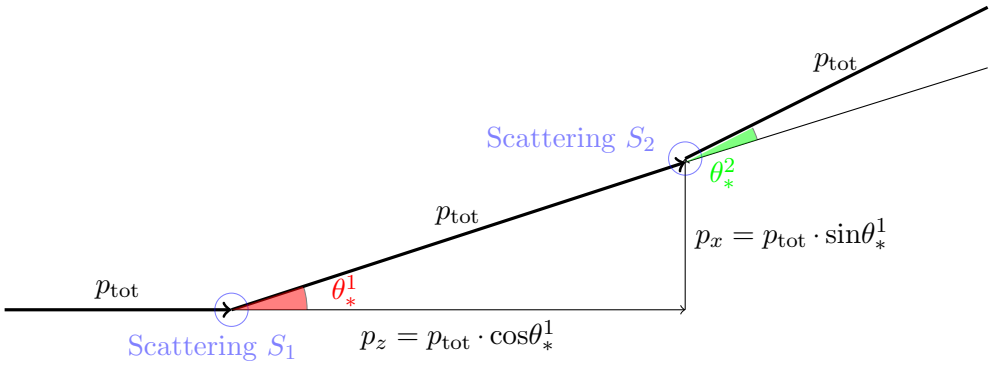

Figure 4: The protons undergoing Coulomb scattering ($\theta_* = \theta_{\text{Coulomb}}$) or Rutherford scattering ($\theta_* = \theta_{\text{Rutherford}}$), rotate about θ_* with regard to the direction of movement as drawn in figure 3.

Before scattering event S_2, the particle's reference system must be adapted to the direction of movement. During the tracking of a particle through a beamline in general, it is not known what happened to the particle before scattering event S_2. However, the phase space coordinates (x, p_x, y, p_y, z, p_z) of each particle are known and the rotation angle θ_*^2 can be estimated as described in section 4.2.2, 4.2.3. Hence, the angle $\Psi_{x,z}$ can be estimated and applied as seen in equation 44.

$$\begin{aligned}
\Psi_{x,z} &= \begin{cases} \arctan\left(\frac{p_x}{p_z}\right) & p_x > 0, \quad p_z > 0 \\ \arctan\left(\frac{p_x}{p_z}\right) + \pi & p_x > 0, \quad p_z < 0 \\ \arctan\left(\frac{p_x}{p_z}\right) + \pi & p_x < 0, \quad p_z < 0 \\ \arctan\left(\frac{p_x}{p_z}\right) + 2\pi & p_x > 0, \quad p_z > 0 \end{cases} \\
p_{\text{tot}} &= \sqrt{p_x^2 + p_z^2}
\end{aligned} \tag{44}$$

$$\rightarrow \begin{pmatrix} p_x \\ p_z \end{pmatrix} = \begin{pmatrix} \cos(\Psi_{x,z}) & \sin(\Psi_{x,z}) \\ -\sin(\Psi_{x,z}) & \cos(\Psi_{x,z}) \end{pmatrix} \cdot \begin{pmatrix} p_{\text{tot}} \cdot \sin\theta_*^2 \\ p_{\text{tot}} \cdot \cos\theta_*^2 \end{pmatrix}$$

The rotation for the p_y, p_z-plane is analogous.

4.3. Verification

To test OPAL on reliability when it comes down to scattering physics, two different schemes with different energies were entered in OPAL and FLUKA. In this section, those schemes are explained and the results of OPAL as well as FLUKA are compared to each other.

4.3.1. Collimator

The first scheme tested is a collimator with a length of 9 cm, made of graphite ($\rho = 2.265$ g/cm^3). For simplicity, the collimator's extent is chosen to be infinitely long in x - and y - direction. The aperture has a length of 3 mm, hence a diameter of 6 mm. Accordingly, the protons send onto this collimator, face a wall of infinite extent with a thickness of 9 cm and a hole with a diameter of 6 mm in it.

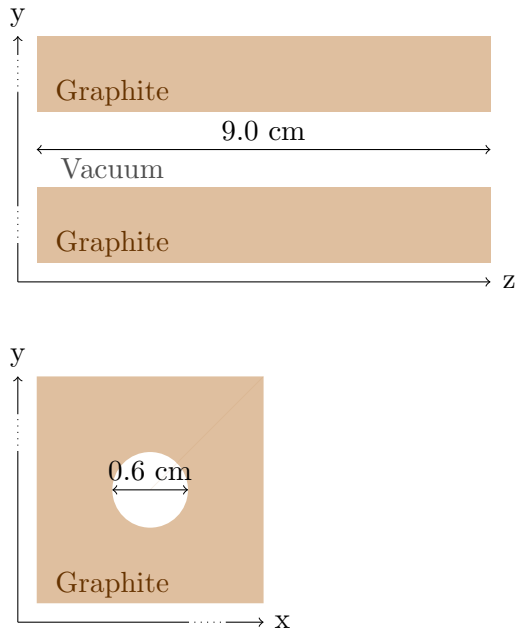

Figure 5: Collimator executed in OPAL and FLUKA, to test the scattering physics implemented in OPAL.

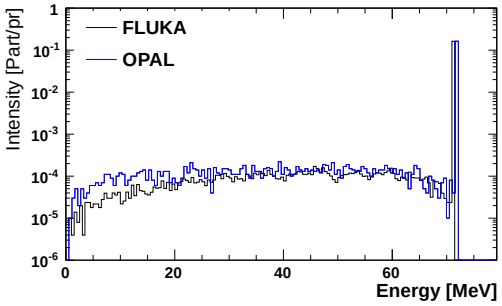

(a) 10^5 protons entered the collimator at an initial energy of 72 MeV.

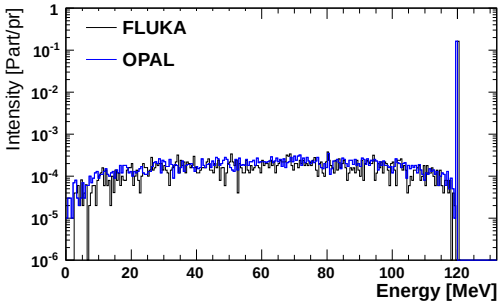

(b) 10^5 protons entered the collimator at an initial energy of 120 MeV.

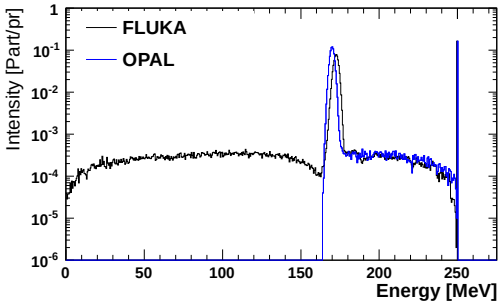

(c) 10^5 protons entered the collimator at an initial energy of 250 MeV.

Figure 6: 10^5 protons initially entered the collimator made of graphite, length 9 cm and a circular opening with a radius of 0.3 cm placed in the center. The blue data is created with FLUKA, whereas the black data is generated with OPAL. The kinetic energy of the protons at the exit of the collimator is plotted versus the normalized intensity.

The transverse proton distribution is initially assumed to be a two-dimensional Gaussian

$$f(x,y) = \frac{1}{2\pi\sigma_x\sigma_y} e^{-\frac{x^2}{2\sigma_x^2} - \frac{y^2}{2\sigma_y^2}}. \qquad (45)$$

with widths $\sigma_x = \sigma_y = 5$ mm. In total, 10^5 protons are sent into the collimator. The peak of this Gaussian is directed onto the opening in the collimator and most particles, placed within this opening, pass the collimator without any scattering at all. However, those particles hitting the wall experience scattering and loose energy with regard to the Bethe-Bloch formula and scatter as described in section 4.

In figure 6, the average kinetic energy of the particles is plotted against the particle intensity. Therefore, the energy axis, starting at zero and ending at the initial kinetic energy each particle enters with, is divided into small bins of approximately 1 MeV. Consequently, the number of protons found in each energy bin, normalized by the initial number of protons entering the collimator, are assigned to the y - axis.

In each of those figures 6a, 6b and 6c, the majority of protons is found at their initial energy of 72 MeV, 120 MeV or 250 MeV. The particles found in `OPAL`, with an energy smaller than their initial energy, agree remarkably well with `FLUKA` in figure 6a and figure 6b. The same can be said for the beam spread seen in figure 7a and figure 7b, where the deflection angle with respect to the z-axis is plotted versus the intensity.

However, protons passing the collimator with an initial energy of 250 MeV show different results. In figure 6c, there are two peaks, one at 250 MeV and the other at 170 MeV. The first peak contains all protons passing the collimator through the vacuum gap, undergoing no scattering. The second peak incorporates all those particles, hitting the wall from the very beginning and passing through the collimator, without seeing the vacuum gap. Those protons degrade according to Bethe-Bloch down to 170 MeV and leave the collimator with a wider spread than protons at a lower initial energy (compare figure 7c to figure 7b and 7a).

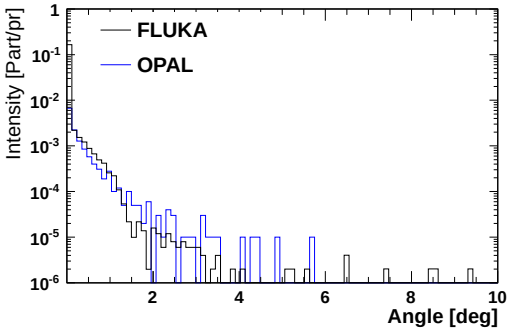

(a) 10^5 protons entered the collimator at an initial energy of 72 MeV,

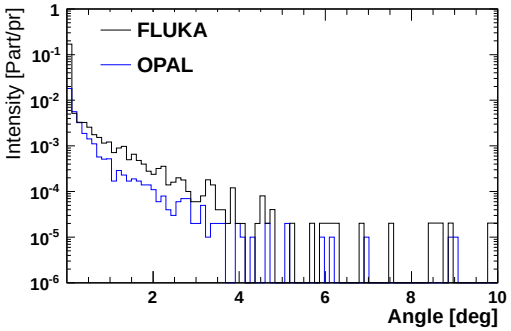

(b) 10^5 protons entered the collimator at an initial energy of 120 MeV.

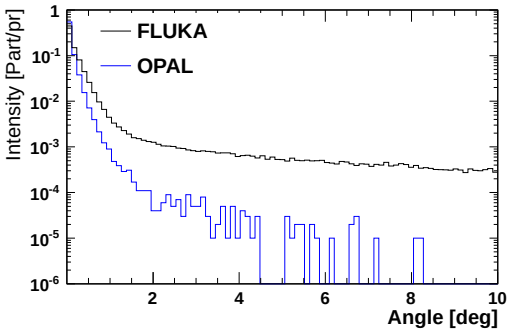

(c) 10^5 protons entered the collimator at an initial energy of 250 MeV.

Figure 7: The blue data is created with `FLUKA`, whereas the black data is generated with `OPAL`. The proton's mean scattering angle, at the exit of the collimator, is plotted with respect to the z-axis versus the normalized intensity.

Outstanding is the difference between the FLUKA and OPAL simulations in figure 6c for energies below 170 MeV. OPAL counts no protons at all on energies below 170 MeV, while FLUKA still encounters 1 to 5 protons per energy bin. This deviation arises from the inelastic scattering implemented in FLUKA but neglected in OPAL.

4.3.2. Degrader

The second scheme tested in OPAL with FLUKA is a degrader made of graphite ($\rho = 2.265$ g/cm^3) with a thickness of 1 cm. Similar to the first scheme tested, the degraders extent is also chosen to be infinitely long. All protons send onto this degrader face a wall of infinite extent with a thickness of 1 cm.

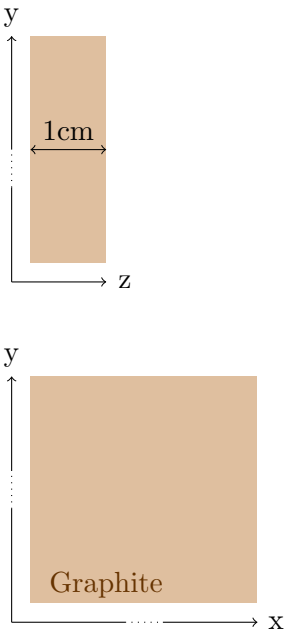

Figure 8: Degrader executed in OPAL and FLUKA to test the scattering physics implemented in OPAL.

Similarly to the collimator as for the degrader, the main peak in figure 9 from the OPAL simulations go accord with the data from FLUKA. However, for energies below the main peak, the OPAL-values always fall behind the data points from FLUKA. The inelastic scattering, implemented in FLUKA but not in OPAL, is accountable for this.

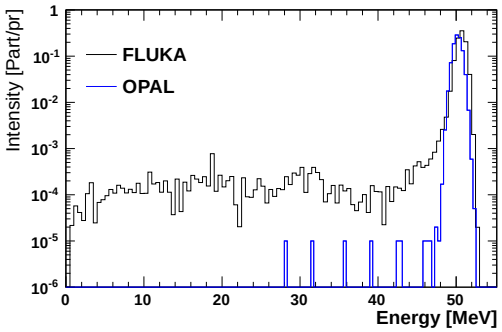

(a) 10^5 protons entered the degrader at an initial kinetic energy of 72 MeV.

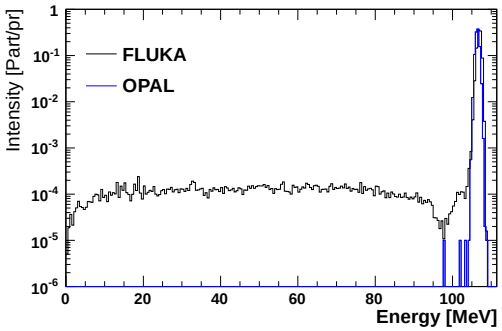

(b) 10^5 protons entered the degrader at an initial kinetic energy of 120 MeV.

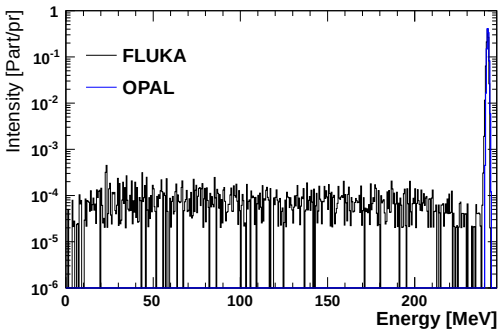

(c) 10^5 protons entered the degrader at an initial kinetic energy of 250 MeV.

Figure 9: A Gaussian bunch of protons, width $\sigma_x = \sigma_y = 3$ mm, entered a degrader made of graphite with length 1 cm. The outgoing protons are plotted blue for the OPAL and black for the FLUKA simulation. The energy is plotted versus the intensity, normalized by the number of incoming protons.

The very first bin in each of the figures 10a, 10b and 10c looks similar for OPAL and FLUKA, hence no meaningful differences between both simulation tools are found for particles experiencing no deflection. Whenever particles do experience deflection, there are constantly more particles deflected in FLUKA than in OPAL. This is also explainable with the generation of secondary protons by inelastic scattering.
To test if the differences between OPAL and FLUKA in figure 7 and 10 really originate from inelastic scattering, two figures are constructed with FLUKA, where the energy is plotted versus the scattering angle. The results show similar behaviour for particles passing a degrader or a collimator, seen in figure 11. There are naturally more particles passing at an energy higher than 170 MeV through the collimator than through the degrader, due to the protons neither undergoing Coulomb nor Rutherford scattering. However, for energies smaller than 170 MeV, both arrangements deliver coinciding results.
The protons arising from inelastic scattering, must have kinetic energies equal or smaller than the kinetic energies of the protons hitting them. For this reasoning, those secondary protons are as well found below 170 MeV as above. For the lack of other physical processes, delivering protons at low kinetic energies, the protons found in the range of 0 MeV - 170 MeV are reasoned to be created by inelastic scattering. Furthermore, the angular proton distribution is fairly uniform for energies below 170 MeV, relying on a scattering process which transfers the bullets momenta unpredictably, delivering in average a smooth angular distribution.
To confirm the insignificance of inelastic scattering for the OPAL-routine regarding a double degrader, it is important to know quantitatively how many protons emerge in the FLUKA routine due to it. The amount of protons leaving the FLUKA-simulation with a kinetic energy below 170 MeV, normalized by the number of initial protons entering (10^5 protons) is:

Collimator	:	3.3%
Degrader	:	4.4%

The protons, leaving the degrader at a wide angular distribution with improper energies, need to be filtered out before entering further medical facilities, most probably with a dipole. At this point, it is safe to say that a proton production of 4.4% is acceptable and the double degrader can be simulated with OPAL, ignoring inelastic scattering.

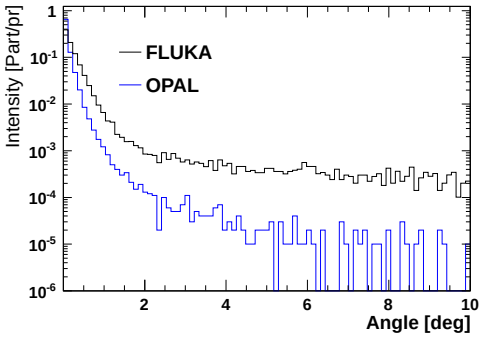

(a) 10^5 protons entered the degrader at an initial kinetic energy of 72 MeV.

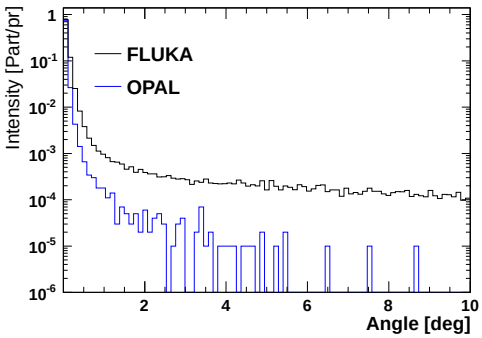

(b) 10^5 protons entered the degrader at an initial kinetic energy of 120 MeV.

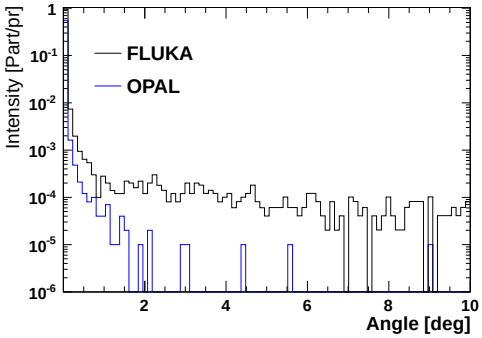

(c) 10^5 protons entered the degrader at an initial kinetic energy of 250 MeV.

Figure 10: A bunch of 10^5 protons entered the degrader head-on with differing initial kinetic energies. For each of those energies, the OPAL data is plotted blue in comparison to the black FLUKA data. The mean scattering angle at the degrader's exit is plotted versus the proton's normalized intensity.

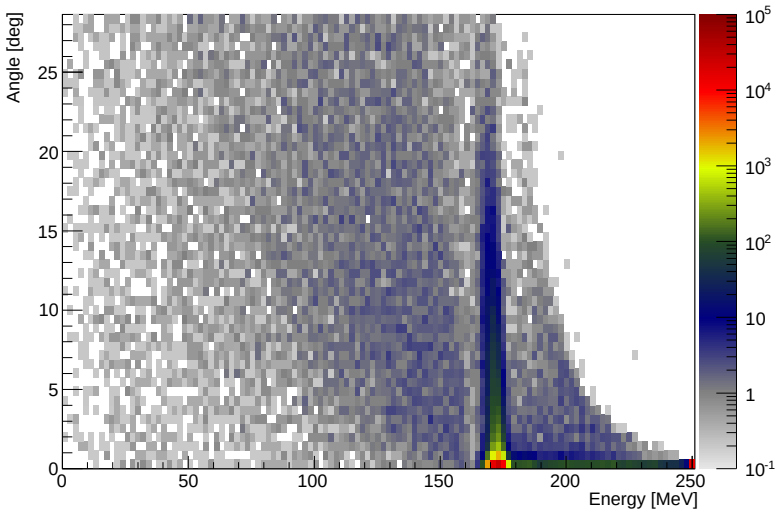

(a) Graphite collimator, as described in figure 5. Most protons leave the collimator without a loss in energy due to scattering at a kinetic energy of 250 MeV. The second peak in intensity is found at a kinetic energy close to 170 MeV, correspondent to the Bethe-Bloch energy loss.

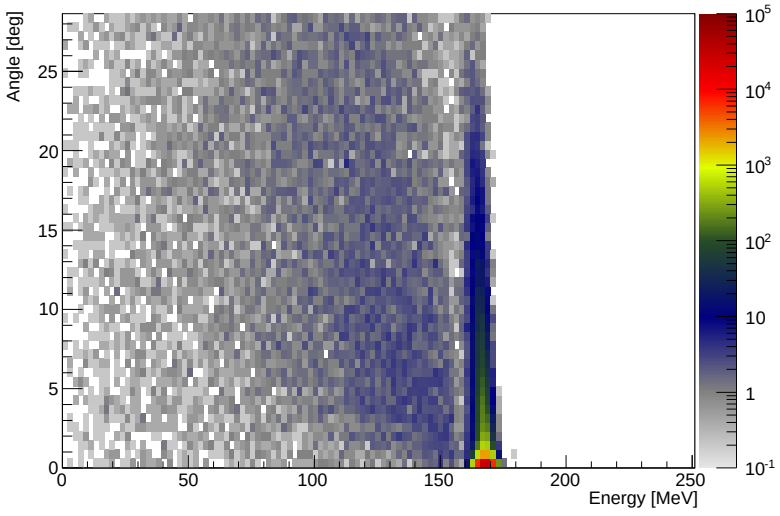

(b) Graphite degrader, similar to the one described in figure 8, but with a thickness of 9 cm. This degrader thickness and material is equivalent to the collimator's thickness and material from figure 11a.

Figure 11: 10^5 protons enter the collimator and the related degrader at an initial kinetic energy of 250 MeV, centrally arranged in a Gaussian with width's $\sigma_x = \sigma_y = 5$ mm. The x-axis shows the kinetic energy of all protons at the collimator's respectively the degrader's exit. The y-axis shows the angle of deflection, the proton leave the arrangement with, regarding the z-axis to be as drawn in figure 5 and 8. The z-axis shows the particles number found for each bin.

5. Double degrader with a quadrupole triplet as focusing element

In order to build a double degrader, a focusing element is needed to place between the two single degraders. The double degrader installation is drawn in figure 12. In order to find a quadrupole triplet fulfilling the matching condition (see equation 20)

$$\sigma^{\text{beam}}_{\text{optimum}} = \frac{\epsilon^{\text{beam}}}{\epsilon^{\text{degrader}}} \cdot \begin{bmatrix} A & B \\ B & C \end{bmatrix} \tag{46}$$

$$= \frac{\epsilon^{\text{beam}}}{\epsilon^{\text{degrader}}} \cdot \epsilon^{\text{degrader}} \cdot \begin{bmatrix} \beta & -\alpha \\ -\alpha & \gamma \end{bmatrix} \tag{47}$$

$$= \epsilon^{\text{beam}} \cdot \begin{bmatrix} \beta & -\alpha \\ -\alpha & \gamma \end{bmatrix}, \tag{48}$$

the sigma matrices of the second degrader (placed at 2.37 m in figure 12) and the beam matrix after the first degradation are needed. With respect to figure 12, we have the following

$$\begin{aligned} \epsilon^{\text{beam}} &= \sqrt{|\sigma^{\text{degrader 1}} + \sigma^{\text{drift}}|} &&= \sqrt{|\sigma_1|} \\ \sigma_1 &= \epsilon^{\text{beam}} \cdot \begin{bmatrix} \beta_1 & -\alpha_1 \\ -\alpha_1 & \gamma_1 \end{bmatrix} &&= \sigma^{\text{degrader 1}} + \sigma^{\text{drift}} \\ \sigma_2 &= \epsilon^{\text{beam}} \cdot \begin{bmatrix} \beta_2 & -\alpha_2 \\ -\alpha_2 & \gamma_2 \end{bmatrix} &&= \sigma^{\text{degrader 2}} + \sigma^{\text{drift}} \\ \sigma^{\text{degrader 2}} &= \begin{bmatrix} A_2 & B_2 \\ B_2 & C_2 \end{bmatrix} &&= \epsilon^{\text{degrader 2}} \cdot \begin{bmatrix} \beta_2^{\text{DEG}} & -\alpha_2^{\text{DEG}} \\ -\alpha_2^{\text{DEG}} & \gamma_2^{\text{DEG}} \end{bmatrix}. \end{aligned}$$

The emittance of the beam, after the first degradation, stays constant when travelling through the quadrupole triplet. However, with the focusing elements, it is possible to adjust

$$\epsilon^{\text{beam}} \cdot \begin{bmatrix} \beta_1 & -\alpha_1 \\ -\alpha_1 & \gamma_1 \end{bmatrix} \rightarrow \epsilon^{\text{beam}} \cdot \begin{bmatrix} \beta_2^{\text{DEG}} & -\alpha_2^{\text{DEG}} \\ -\alpha_2^{\text{DEG}} & \gamma_2^{\text{DEG}} \end{bmatrix}, \tag{49}$$

such that the beam matrix at end of the second degrader fulfills the matching condition. The Twiss parameters always fulfill $\beta\gamma - \alpha^2 = 1$. For that reason, adjusting them after the first degrader to the matching condition has no impact on the beam emittance, before the beam enters the second degrader.

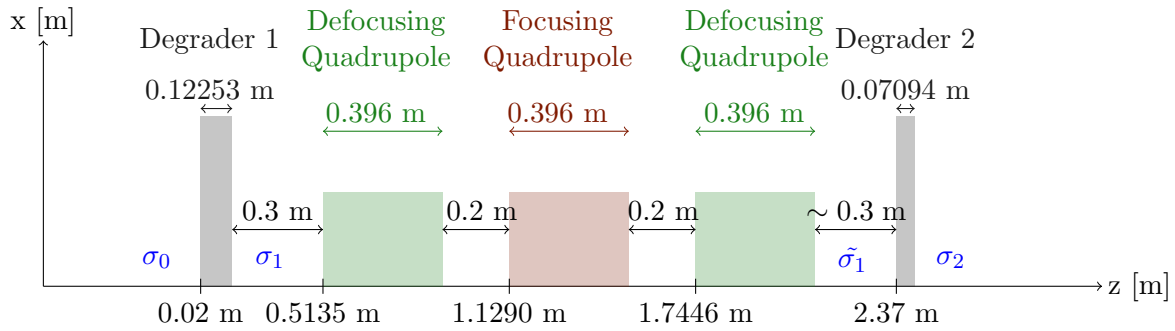

Figure 12: The double degrader installation as simulated with `OPAL`. The widths are estimated either with `MADX` or in private communication with Dr. Christian Baumgarten. The final separation between the last quadrupole and the second degrader is marked with a tilde to indicate small adjustments, estimated with some experimentation in `OPAL`. Moving the final degrader about several millimeters can already change the output beam positively in dependence on the beam focus.

5.1. First degrader

The very first information needed is the thickness of the first degrader, hence the energy the protons should have after the first degradation. Ideally, the protons should have an equal growth in emittance in both degraders, $\epsilon_1^{\text{DEG}} = \epsilon_2^{\text{DEG}}$ to get $\epsilon_{\text{out}} = \epsilon^0 + \epsilon_1^{\text{DEG}} + \epsilon_2^{\text{DEG}}$ minimized.
Dr. Farley estimated the gain in intensity for a double degrader, compared to a conventional degrader, to be a factor 2 for each transverse direction. This means, the sum of degrader emittances should be 2 times smaller than for a conventional degrader

$$\frac{\epsilon_{\text{conventional}}^{\text{DEG}}}{2} = \epsilon_1^{\text{DEG}} + \epsilon_2^{\text{DEG}} = 2\epsilon_1^{\text{DEG}} \;\rightarrow\; \epsilon_1^{\text{DEG}} = \frac{\epsilon_{\text{conventional}}^{\text{DEG}}}{4}. \tag{50}$$

At this point it is time to look into Dr. Baumgarten's work [Bau13], briefly described in section 3.2. Dr. Baumgarten has written a program, which calculates, with the help of a Runge-Kutta Integration, the energy a particle looses when travelling through material. Additionally, the beam emittance and the corresponding sigma matrix are estimated. The physics implemented in this program is described in section 2.1.1 and section 4.1.1 and relies on Dr. Farley's framework. The program's outcome for a degradation of protons from an energy of 250 MeV to 72 MeV, by passing through graphite with a density of $\rho = 2.210\ \text{g/cm}^3$, can be seen in figure 13. According to this Runge-Kutta scheme, the first degrader should have a thickness of 0.110 m, degrading the protons from 250 MeV to 155 MeV. To check on those values, a similar degrader is implemented in `OPAL`. So far, the input emittance in the Runge-Kutta scheme is to zero. In order to compare the results from `OPAL` to the Runge-Kutta scheme, the input emittance in `OPAL` is also assumed to be zero for the time being.

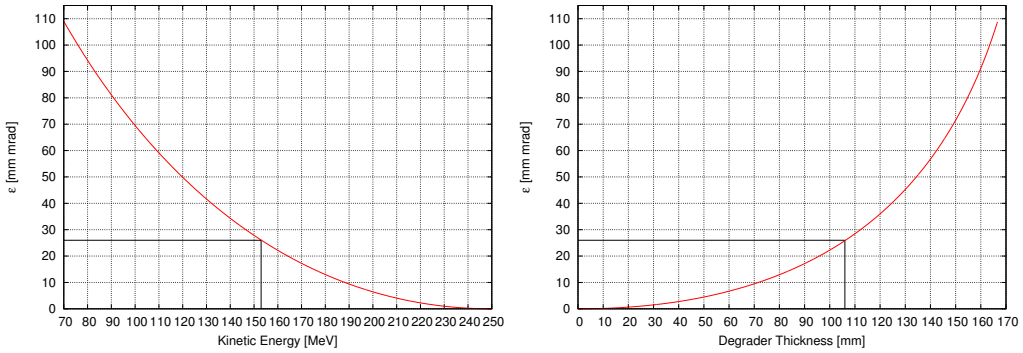

(a) Kinetic energy versus beam emittance. (b) Degrader thickness versus beam emittance

Figure 13: The kinetic energy and the degrader thickness are plotted versus the beam emittance. This data is calculated for protons, degraded from 250 MeV to 72 MeV, with Dr. Baumgarten's Runge Kutta program. The black lines mark the position of ϵ_1^{DEG} and the kinetic energy loss, respectively the material thickness associated with it.

For comparison, a similar degrader is simulated with `OPAL`. However, the density pre-implemented in `OPAL` is $\rho = 2.210\ \text{g/cm}^3$, which differs slightly from the density used in [Bau13]. For this reason, I felt free to ask Dr. Baumgarten for his Runge-Kutta scheme and found for the density implemented in `OPAL`, with the help of his program, the sigma matrix

$$\sigma^{\text{degrader 1}}_{\rho=2.210\ \text{g/cm}^3} = \begin{pmatrix} 2.527\ \text{mm}^2 & 38.073\ \text{mm mrad} \\ 38.073\ \text{mm mrad} & 831.642\ \text{mrad}^2 \end{pmatrix}. \tag{51}$$

This sigma matrix corresponds to the scattering matrix at the end of the first degrader slab of thickness 110 mm, degrading protons from 250 MeV to 155 MeV.

Dr. Baumgarten estimated the thickness of the first degrader to be 110 mm in order to degrade the protons to 155 MeV. Some experimentation in `OPAL` delivers a shorter thickness of 104.6 mm and the

beam matrix

$$\begin{aligned}\sigma_x^{\text{beam}} &= \begin{pmatrix} 2.401 \pm 0.18 \text{ mm}^2 & 34.07 \pm 0.7311 \text{ mm mrad} \\ 34.07 \pm 0.7311 \text{ mm mrad} & 655.5 \pm 7.481 \text{ mrad}^2 \end{pmatrix} \\ &= 20.32 \pm 1.848 \text{ mm mrad} \cdot \begin{pmatrix} 0.1181 \pm 0.01392 \text{ mm/mrad} & -1.676 \pm -0.1566 \\ -1.676 \pm -0.1566 & 32.25 \pm 2.956 \text{ mrad/mm} \end{pmatrix}\end{aligned} \tag{52}$$

The scattering physics implemented in the Runge-Kutta (described in section 2.1.1), incorporates material characteristics by introducing the material dependent factor $K = 200 \cdot \frac{Z^2}{X_0}$. In `OPAL` is the scattering physics implemented differently and accommodates the material characteristics through the projected angle $\alpha(\theta_0)$ with $\theta_0 = \frac{13.6 \text{ MeV}}{\beta cp} z \sqrt{\Delta s / X_0} \left[1 + 0.038 \ln \Delta s / X_0\right]$. As both methods differ in implementation, they deliver unequal material lengths.

Consequently, as `OPAL` has a shorter degrader length, the corresponding σ_{xx},σ_{xp_x} and $\sigma_{p_x p_x}$ are also smaller. The values from the simulation are systematically smaller about a factor ~ 1.3, resulting in quantitatively similar behaviour for scattering processes. Hence, regarding the completely different solving schemes (Runge-Kutta integration versus a tracking simulation), the matrices agree with each other reasonably.

5.1.1. Choice of material

Dr. Baumgarten and Dr. Pedroni chose to investigate the passage of protons through graphite with a density of $\rho = 2.265$ g/cm^3. This is a good choice for testing Dr. Farley's method on general reliability. However, when it comes down to realistic applications, graphite with $\rho = 2.265$ g/cm^3 is not producible in the means of a double degrader. Although, graphite with a density of $\rho = 1.88$ g/cm^3 is achievable and already in use at PSI. For that reason, the degrader material investigated any further, has density $\rho = 1.88$ g/cm^3. The Runge-Kutta scheme delivers slightly different results for a density of $\rho = 1.88$ g/cm^3 and so does `OPAL`. The thickness needed for the first degrader in the double degrader setup is estimated once with the Runge-Kutta scheme and reassessed with `OPAL`. The results are listed in table 2.
The values from `OPAL` are consistently smaller than the values from the Runge-Kutta scheme, but behave quantitatively similar. The emittance for the degradation from 250 MeV to 72 MeV equals four times the emittance of the first degrader slab, slowing the protons down from 250 MeV to 154.77 MeV. Additionally, the emittance from the first degrader added to the emittance from the second degrader, delivers half the emittance of the thick degrader.

5.1.2. Realistic input emittance

So far an input emittance equal to zero was used, which enforces a point-like proton distribution. The initial input emittance delivered by the cyclotron COMET is small and will be close to zero, when compared to the emittance exiting from the first degrader. From that point of view, a zero input emittance is eligible. However, in this simulation more realistic boundaries are applied:

$$\begin{array}{lllllll} \delta_x & = & 0.503 & & \delta_y & = & 0.858 \\ \sigma_x & = & 0.83 \text{ mm} & & \sigma_y & = & 0.987 \text{ mm} \\ \sigma_{p_x} & = & 0.743 \text{ mrad} & & \sigma_{p_y} & = & 0.646 \text{ mrad} \end{array}$$

These are the values describing the proton beam distribution emerging from the cyclotron COMET, which is in use for proton therapy at PSI at present. In a private communication with Dr. Baumgarten, those values came up and are used as a non-zero input emittance for further simulations discussed in this report.
Regarding table 2, the values emerging from simulations with the realistic input emittance, are in

general larger than the analogous values assuming zero input emittance. However, the OPAL values in general are smaller than the values from the Runge-Kutta scheme.

	thickness	input E_{kin}	output E_{kin}	emittance
Runge-Kutta	200.7 mm	250 MeV	72 MeV	127.4 mm mrad
	126.2 mm	250 MeV	154.77 MeV	31.85 mm mrad
	73.4 mm	154.77 MeV	72 MeV	30.998 mm mrad
OPAL (initial proton distribution is point like)	193.468 mm	250 MeV	72 MeV	93.94 mm mrad
	122.53 mm	250 MeV	154.77 MeV	23.56 mm mrad
	70.938 mm	154.77 MeV	72 MeV	22.2 mm mrad
OPAL (initial proton distribution is a Gaussian)	193.468 mm	250 MeV	72 MeV	$\epsilon_x = 102.48$ mm mrad $\epsilon_y = 103.54$ mm mrad
	122.53 mm	250 MeV	154.77 MeV	$\epsilon_x = 33.66$ mm mrad $\epsilon_y = 34.94$ mm mrad
	70.938 mm	154.77 MeV	72 MeV	$\epsilon_x = 38.09$ mm mrad $\epsilon_y = 40.04$ mm mrad

Table 2: The values from Dr. Baumgarten's Runge-Kutta scheme are compared to the corresponding OPAL values, where both methods assume zero input emittance. The OPAL values with zero input emittance are subsequently compared to OPAL values, where the realistic initial proton distribution from COMET is used. All values listed here are estimated with a graphite density of $\rho = 1.88$ g/cm^3.

5.2. Quadrupole triplet

5.2.1. Matching in MADX

In order to fulfil the matching condition 20, focusing elements can adjust the Twiss parameters emerging from the first degrader accordingly(see equation 49)

$$\begin{aligned} \alpha_x &= -1.054 && \text{to} \quad \alpha_x = -1.3499 \\ \alpha_y &= -1.011 && \text{to} \quad \alpha_y = -1.3499 \\ \beta_x &= 0.10958 \text{ mm/mrad} && \text{to} \quad \beta_x = 0.0586 \text{ mm/mrad} \\ \text{and} \quad \beta_y &= 0.10855 \text{ mm/mrad} && \text{to} \quad \beta_y = 0.0586 \text{ mm/mrad.} \end{aligned}$$

The values on the left side are the Twiss parameters belonging to the beam matrix emerging from the first degrader in the double degrader setup, drawn in figure 12. The Twiss parameters on the right side result from the Runge Kutta scheme, applied on protons travelling in graphite with a density of $\rho = 1.88$ g/cm^3 and thickness 122.53 mm.
There are several programs able to compute the requested focusing strengths. The program used here is called MADX [AoC13], an acronym for **m**ethodical **a**ccelerator **d**esign. Besides the Twiss values, MADX needs more input values such as

$$\begin{aligned} \sigma_x &= 1.920 \text{ mm} && \sigma_y = 1.947 \text{ mm} \\ \sigma_{p_x} &= 25.468 \text{ mrad} && \sigma_{p_y} = 25.511 \text{ mrad} \\ E_{\text{kinetic}} &= 154.77 \text{ MeV} \end{aligned}$$

to compute the correct focusing strengths. Those input values for MADX are taken from the beam matrix emerging from the first degrader of the double degrader setup, seen in figure 12 and simulated with OPAL. Alongside with the beam distribution, some restrictions must be set on the double degrader setup to let MADX do the matching. The restrictions are already drawn in figure 12:

- Technically, it is not possible to place the first quadrupole directly against the first degrader. There must be a minimum space of roughly 30 cm.

- The quadrupoles can not be placed directly against each other either. There needs to be a minimum separation of roughly 20 cm.
- The length of the entire setup should be as short as possible, to save on construction costs, material and maintenance.

Provided with these input values and restrictions, `MADX` version 5.01.00 delivers the focusing strengths listed in table 3 and plotted in figure 14. Additionally to the focusing strengths, `MADX` computes the length of each quadrupole to be 395.58 mm.

first quadrupole:	K	=	-	14.924 T/m
second quadrupole:	K	=		15.137 T/m
third quadrupole:	K	=	-	17.607 T/m.

Table 3: The quadrupole's focusing strengths computed with `MADX`, are listed. A quadrupole with a positive focusing strengths is focusing in x-direction and defocusing in y-direction. It works the opposite way around for a quadrupole with a negative focusing strength.

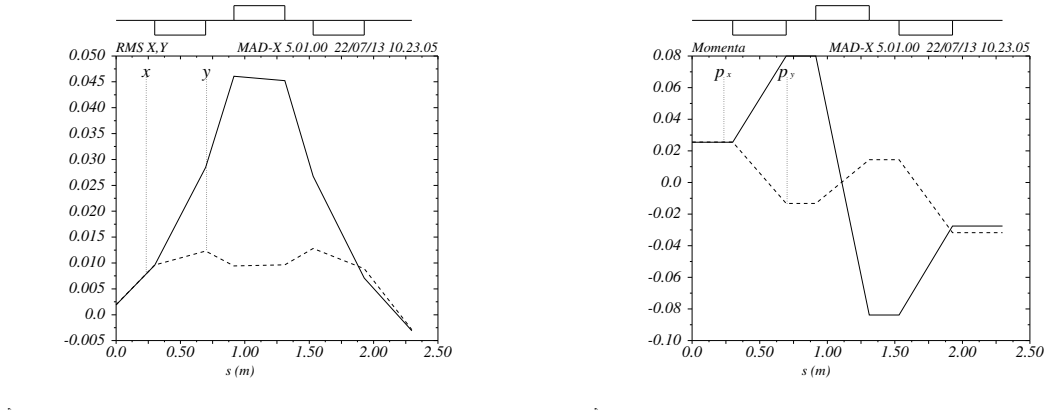

Figure 14: `MADX` delivers the focusing strengths listed in table 3 and this plot, showing the behaviour of protons travelling through such a quadrupole triplet. The figure on the left shows σ_x and σ_y. The protons are firstly focused in y-direction, then focused in x-direction and finally refocused in y-direction. As the x-direction becomes defocused at first, σ_x blows up to 4.5 cm.

5.2.2. Implementation in `OPAL`

The units used in `MADX` differ from the ones in `OPAL`, hence the results from `MADX` need to be converted accordingly, before being entered in `OPAL`. I shall not go into detail about these conversions, but for the interested reader, they are written down in a "cheat sheet", which is appended to this report in appendix A.

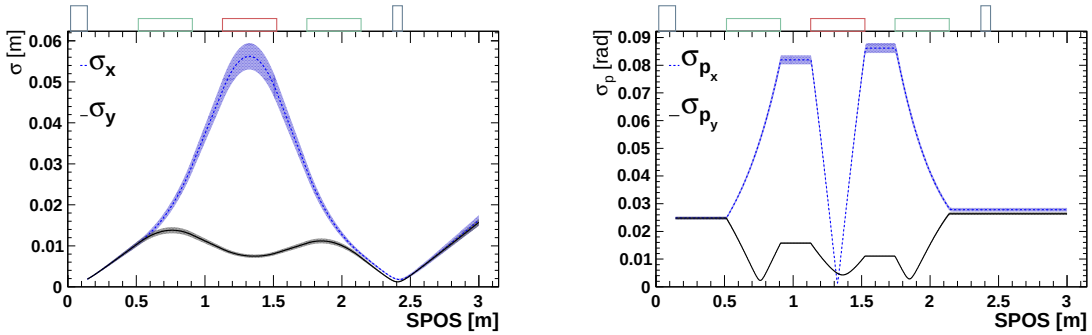

Figure 15: The data plotted here is generated with OPAL, with focusing strengths slightly altered from the ones estimated in MADX. The coloured blocks on the top of each plot indicate where the degraders would be placed and where the quadrupoles are placed. The green blocks denote a in x-direction defocusing, the red block a focusing quadrupole. The grey blocks indicate degraders, where in this plot only the first degrader on the left side is partially taken into account. The proton distribution emerging from the first degrader, simulated with OPAL, is used as an input proton distribution for the quadrupole triplet. The energy distribution emerging from the first degrader is a Gaussian distribution, which is not used here. Instead, all protons inserted into the quadrupole triplet possess a kinetic energy of 154.77 MeV. The errors of σ_x and σ_{p_x} (see section B.1.1) are also plotted.

To check on the focusing dynamics firstly, the quadrupole triplet is only implemented in OPAL. The proton distribution emerging from the first degrader, simulated with OPAL, is used as an input distribution for the quadrupole triplet. The energy entering the quadrupole triplet is chosen to be a delta peak. All protons entering the quadrupole triplet in this first quadrupole simulation have exactly an energy of 154.77 MeV, whereas the energy distribution emerging from the first degrader is a Gaussian distribution. This is done for simplicity and needs to be taken into account for further insight. The focusing strengths estimated with MADX deliver a good focusing in the OPAL simulations, but some experimentation in OPAL delivers even better focusing. The results of this experimentation can be seen in figure 15. The focusing strengths delivered by MADX are slightly modified and listed in table 4. These altered focusing strengths are used in upcoming simulations done in OPAL, with regard to the double degrader.

first quadrupole:	K	=	-	14.700 T/m
second quadrupole:	K	=		15.008 T/m
third quadrupole:	K	=	-	17.343 T/m.

Table 4: The quadrupole strengths estimated by MADX are slightly modified to use in OPAL. The altered values are listed here.

The correlation matrix after the quadrupole triplet at $z = 2.4$ m takes the following form

$$\begin{aligned}
\sigma_x^{\text{beam}} &= \begin{pmatrix} 3.65 \pm 0.08026 \text{ mm}^2 & -14.74 \pm 0.2756 \text{ mm mrad} \\ -14.74 \pm 0.2756 \text{ mm mrad} & 766.9 \pm 3.419 \text{ mrad}^2 \end{pmatrix} \\
&= 50.82 \pm 0.3453 \text{ mm mrad} \cdot \begin{pmatrix} 0.07183 \pm 0.001653 \text{ mm/mrad} & 0.29 \pm 0.005769 \\ 0.29 \pm 0.005769 & 15.09 \pm 0.1226 \text{ mrad/mm} \end{pmatrix} \\
\sigma_y^{\text{beam}} &= \begin{pmatrix} 1.638 \pm 0.01769 \text{ mm}^2 & -5.348 \pm 0.09119 \text{ mm mrad} \\ -5.348 \pm 0.09119 \text{ mm mrad} & 724.8 \pm 2.788 \text{ mrad}^2 \end{pmatrix} \\
&= 34.04 \pm 0.1106 \text{ mm mrad} \cdot \begin{pmatrix} 0.04812 \pm 0.0005428 \text{ mm/mrad} & 0.1571 \pm 0.002727 \\ 0.1571 \pm 0.002727 & 21.29 \pm 0.1072 \text{ mrad/mm} \end{pmatrix}
\end{aligned} \tag{53}$$

which is not preserving the emittance in x-direction, as the emittance leaving the first degrader (and used as an input emittance for the quadrupole triplet) is $\epsilon_x = 33.66$ mm mrad. When looking at the correlation matrix in figure 16, it becomes clear, why the emittance $\epsilon_x^{\text{rms}} = \sqrt{\sigma_{xx}\sigma_{p_xp_x} - \sigma_{xp_x}^2}$ is not preserved. The correlation values δ_{xp_z}, $\delta_{p_xp_z}$, δ_{yp_z} and $\delta_{p_yp_z}$ are not zero. These correlation values indicate dispersion, which needs to be included into the emittance calculation.

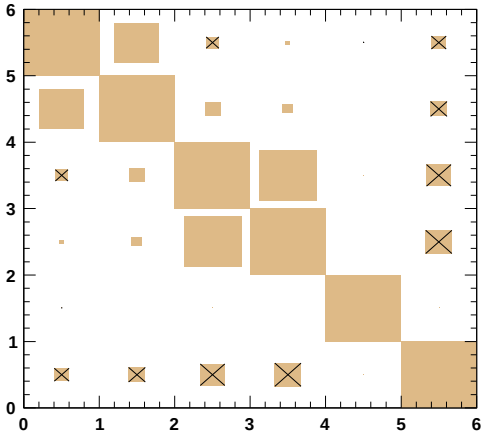

Figure 16: This is the correlation matrix of the quadrupole triplet simulation for all protons captured in a monitor placed at $z = 2.439$ m. We see correlation values unequal to zero for δ_{xp_z}, $\delta_{p_xp_z}$, δ_{yp_z} and $\delta_{p_yp_z}$.

5.3. Double degrader with Gaussian energy distribution

The double degrader installation drawn in figure 12, with the monitors from figure 23, is simulated with `OPAL`. 10^5 protons are tracked through this installation. They start with a kinetic energy of 250 MeV and become firstly degraded to 154.77 MeV. Subsequently, a quadrupole triplet focuses the beam onto the second degrader in accordance with the matching condition (formula 20). Lastly, the protons travel through the second degrader and end up at a kinetic energy of 72 MeV. The results of `OPAL`'s tracking in time are shown in figure 17. The correlation matrices from the monitors placed behind the first and second degrader as well as in front of the second degrader, are listed and plotted beforehand in section B.

Roughly, the results from this `OPAL`-simulation go accord with the simulation of the quadrupole triplet shown in figure 15. Nevertheless, the focusing for the double degrader is worse than for the simulation of the quadrupole triplet only. Before entering the second degrader, neither the standard deviation of the space nor of the momenta distribution in x- and y-direction do clash.

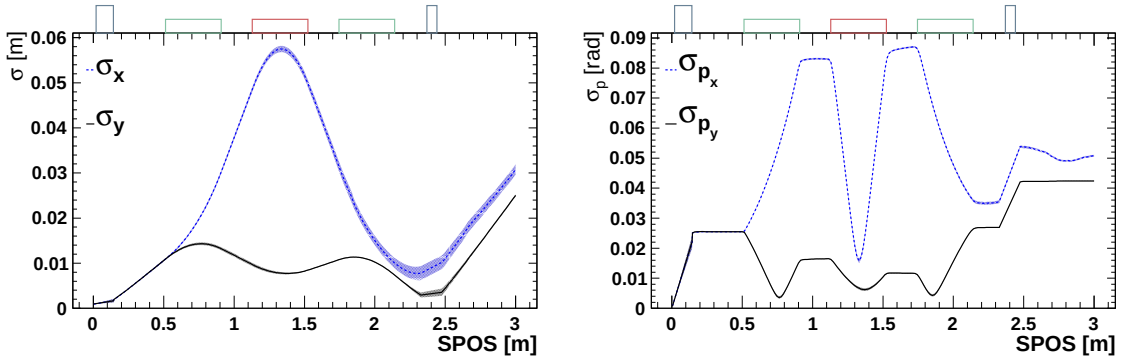

(a) Standard deviation of the space distribution: σ_x and σ_y from formula 61.

(b) Standard deviation of the momenta distribution: σ_{p_x} and σ_{p_y} from formula 62.

Figure 17: `OPAL` simulation of 10^5 protons travelling through the double degrader installation drawn in figure 12. These plots show `OPAL`'s tracking in time.

The sigma distribution in the (x, p_x)- and (y, p_y)-plane, captured in a monitor placed right before the second degrader, at $z = 2.368$ m , takes the form

$$\begin{aligned}
\sigma_x^{\text{beam}} &= \begin{pmatrix} 56.77 \pm 21.44 \text{ mm}^2 & 82.03 \pm 12.47 \text{ mm mrad} \\ 82.03 \pm 12.47 \text{ mm mrad} & 973.2 \pm 17.73 \text{ mrad}^2 \end{pmatrix} \\
&= 220.3 \pm 24.84 \text{ mm mrad} \cdot \begin{pmatrix} 0.2577 \pm 0.1016 \text{ mm/mrad} & -0.3724 \pm -0.07048 \\ -0.3724 \pm -0.07048 & 4.418 \pm 0.5047 \text{ mrad/mm} \end{pmatrix} \\
\sigma_y^{\text{beam}} &= \begin{pmatrix} 3.038 \pm 0.2835 \text{ mm}^2 & -27 \pm 0.3536 \text{ mm mrad} \\ -27 \pm 0.3536 \text{ mm mrad} & 716.9 \pm 5.328 \text{ mrad}^2 \end{pmatrix} \\
&= 38.06 \pm 1.368 \text{ mm mrad} \cdot \begin{pmatrix} 0.07981 \pm 0.007982 \text{ mm/mrad} & 0.7094 \pm 0.02714 \\ 0.7094 \pm 0.02714 & 18.83 \pm 0.6914 \text{ mrad/mm} \end{pmatrix}
\end{aligned} \tag{54}$$

It is not possible to place the second monitor inside the degrader, right on the focus of the quadrupole triplet. Nevertheless, this monitor is very close to the second degrader, thus close to the focusing point. Consequently, the Twiss parameters of the two beam matrices should be similar to each other and approximate the Twiss parameters (listed in section 5.2.1) $\alpha = -1.3499$, $\beta = 0.0586$ mm/mrad and $\gamma = 48.1609$ mrad/mm, fulfilling the matching condition(equation 20). Unfortunately, the Twiss Parameters from the beam matrices gathered at the second monitor are not alike to the ones pursued. Furthermore, as indicated in section B, the correlation matrix has two correlation values being unexpectedly not close to zero: $\delta_{xp_z} = -0,162$ and $\delta_{p_x,p_z} = -0,0526$.

5.3.1. Output emittance

The data points captured in monitor 3 placed at 2.442 m delivers a beam matrix σ^2 (with regard to figure 23)

$$\begin{aligned}
\sigma_x^{\text{beam}} &= \begin{pmatrix} 48.35 \pm 8.579 \text{ mm}^2 & 139.5 \pm 3.767 \text{ mm mrad} \\ 139.5 \pm 3.767 \text{ mm mrad} & 1960 \pm 6.459 \text{ mrad}^2 \end{pmatrix} \\
&= 274.4 \pm 15.53 \text{ mm mrad} \cdot \begin{pmatrix} 0.1762 \pm 0.03282 \text{ mm/mrad} & -0.5084 \pm -0.03187 \\ -0.5084 \pm -0.03187 & 7.142 \pm 0.4048 \text{ mrad/mm} \end{pmatrix} \\
\sigma_y^{\text{beam}} &= \begin{pmatrix} 4.386 \pm 0.2859 \text{ mm}^2 & 57.2 \pm 0.472 \text{ mm mrad} \\ 57.2 \pm 0.472 \text{ mm mrad} & 1785 \pm 5.096 \text{ mrad}^2 \end{pmatrix} \\
&= 67.51 \pm 1.938 \text{ mm mrad} \cdot \begin{pmatrix} 0.06497 \pm 0.004628 \text{ mm/mrad} & -0.8473 \pm -0.02531 \\ -0.8473 \pm -0.02531 & 26.44 \pm 0.7628 \text{ mrad/mm} \end{pmatrix}
\end{aligned} \tag{55}$$

The emittance captured in this monitor thus equals:

$$\begin{aligned} \epsilon_x^{1\sigma} &= 274.4 \pm 15.53 \text{ mm mrad} \\ \epsilon_y^{1\sigma} &= 67.51 \pm 1.938 \text{ mm mrad} \end{aligned}$$

Those emittances are not as good as Dr. Baumgarten's optimal emittance, which in this case would be

$$\frac{\epsilon^{\text{DEG}}_{\text{conventional}}}{2} = \begin{cases} 51,24 \text{ mm mrad} & x \text{ direction} \\ 51,77 \text{ mm mrad} & y \text{ direction} \end{cases} \tag{56}$$

5.4. Double degrader with cut in energy

The discrepancies between the expected and the simulated beam matrix of the double degrader may originate from the energy distribution emerging the first degrader. Not all particles become degraded identically. In large parts, the protons degrade closely to 154.77 MeV, in accordance to the Bethe-Bloch formula 24. However, not all particles travel exactly the same length of path inside the graphite, as they do Coulomb and Rutherford scattering (see section 4.1.2). Different lengths of path lead to different losses in energy, hence a bunch of protons with a continuous energy distribution leaves the first degrader. The quadrupole triplet can not accommodate the distribution in kinetic energy, but is designed for exactly the kinetic energy of 154.77 MeV. In practice, this problem is solved by placing a dipole right behind the first degrader, to only let pass the particles at the desired energy. All other particles get deflected too heavily or too weakly and become absorbed in a collimator. To imitate this procedure, the protons leaving the first degrader are dumped with their phase space coordinates in a file. Those protons are consequently analysed on their kinetic energy. Only protons with a kinetic energy in the range of 154.77 MeV $\pm$ 1.5477 MeV are passed back into the double degrader. The result of this treatment is plotted in figure 18 and shows a focusing far more similiar to the quadrupole triplet seen in figure 15. The standard deviations of the space and the momenta distribution in x- and y-direction match to each other after the first degrader and stay aligned for at least 0.5 m.

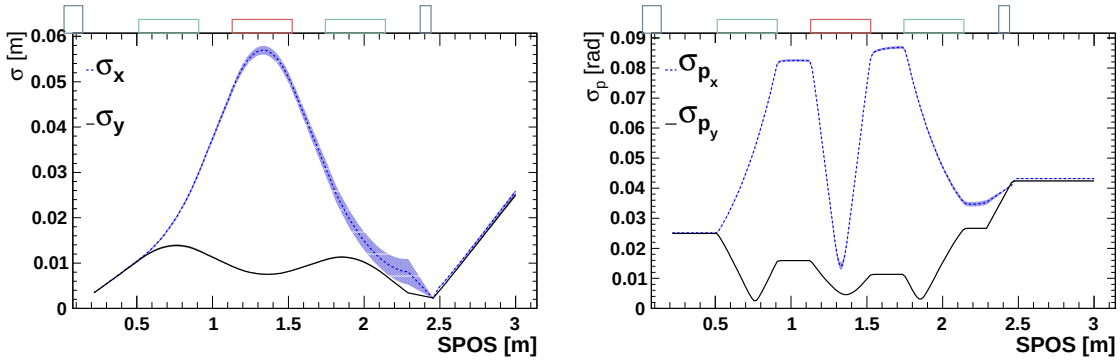

(a) Standard deviation of the distribution: σ_x and σ_y from formula 61.

(b) Standard deviation of the distribution: σ_{p_x} and σ_{p_y} from formula 62.

Figure 18: `OPAL` simulation of 10^5 protons travelling the double degrader installation. In addition to the previous simulation shown in figure 17, a selection on the protons energy distribution is applied after the first degrader. Only protons with an energy of 154.77 MeV $\pm$ 1.5477 MeV are allowed to proceed into the quadrupole triplet. This improves the beam focusing.

From the initial 10^5 protons, only 38248 have an energy within 154.77 MeV $\pm$ 1.5477 MeV, after the first degrader. Those are admitted into the quadrupole triplet and produce a beam matrix at the second monitor, placed at 2.368 m:

$$\begin{aligned}
\sigma_x^{\text{beam}} &= \begin{pmatrix} 8.784 \pm 1.013 \text{ mm}^2 & -9.869 \pm 1.824 \text{ mm mrad} \\ -9.869 \pm 1.824 \text{ mm mrad} & 788 \pm 8.624 \text{ mrad}^2 \end{pmatrix} \\
&= 82.61 \pm 2.6 \text{ mm mrad} \cdot \begin{pmatrix} 0.1063 \pm 0.01272 \text{ mm/mrad} & 0.1195 \pm 0.0224 \\ 0.1195 \pm 0.0224 & 9.539 \pm 0.3178 \text{ mrad/mm} \end{pmatrix} \\
\sigma_y^{\text{beam}} &= \begin{pmatrix} 2.64 \pm 0.05402 \text{ mm}^2 & -27.11 \pm 0.3567 \text{ mm mrad} \\ -27.11 \pm 0.3567 \text{ mm mrad} & 710.9 \pm 8.297 \text{ mrad}^2 \end{pmatrix} \\
&= 33.79 \pm 0.4475 \text{ mm mrad} \cdot \begin{pmatrix} 0.07814 \pm 0.001904 \text{ mm/mrad} & 0.8024 \pm 0.01498 \\ 0.8024 \pm 0.01498 & 21.04 \pm 0.3713 \text{ mrad/mm} \end{pmatrix}
\end{aligned} \tag{57}$$

The monitor right after the second degrader at 2.442 m records the beam matrix:

$$\begin{aligned}
\sigma_x^{\text{beam}} &= \begin{pmatrix} 11.08 \pm 1.445 \text{ mm}^2 & 73.21 \pm 1.485 \text{ mm mrad} \\ 73.21 \pm 1.485 \text{ mm mrad} & 1861 \pm 10.63 \text{ mrad}^2 \end{pmatrix} \\
&= 123.5 \pm 5.552 \text{ mm mrad} \cdot \begin{pmatrix} 0.08969 \pm 0.01238 \text{ mm/mrad} & -0.5927 \pm -0.02923 \\ -0.5927 \pm -0.02923 & 15.07 \pm 0.6826 \text{ mrad/mm} \end{pmatrix} \\
\sigma_y^{\text{beam}} &= \begin{pmatrix} 3.886 \pm 0.1549 \text{ mm}^2 & 56.54 \pm 0.6372 \text{ mm mrad} \\ 56.54 \pm 0.6372 \text{ mm mrad} & 1797 \pm 9.63 \text{ mrad}^2 \end{pmatrix} \\
&= 61.52 \pm 1.289 \text{ mm mrad} \cdot \begin{pmatrix} 0.06316 \pm 0.002844 \text{ mm/mrad} & -0.919 \pm -0.02186 \\ -0.919 \pm -0.02186 & 29.21 \pm 0.6315 \text{ mrad/mm} \end{pmatrix}
\end{aligned} \tag{58}$$

The correlation matrices of the double degrader with a selection in energy after the first degrader, look better than the matrices where no energy selection is applied. This time, there are no correlation values, δ_{xp_z} or $\delta_{p_xp_z}$ significantly greater zero, as can be seen in figure 19. Although the emittance after the second degrader is smaller with the cut in energy, one question remains unanswered. The beam emittance does not stay constant when travelling the quadrupole triplet. Before entering the quadrupole triplet, the beam emittance is

$$\begin{aligned}
\epsilon_x^{1\sigma} &= 32.81 \pm 42.25 \text{ mm mrad} \\
\epsilon_y^{1\sigma} &= 33.56 \pm 31.79 \text{ mm mrad}
\end{aligned}$$

After the quadrupole triplet, before entering the second degrader, the emittance is

$$\begin{aligned}
\epsilon_x^{1\sigma} &= 82.61 \pm 2.6 \text{ mm mrad} \\
\epsilon_y^{1\sigma} &= 33.79 \pm 0.4475 \text{ mm mrad}
\end{aligned}$$

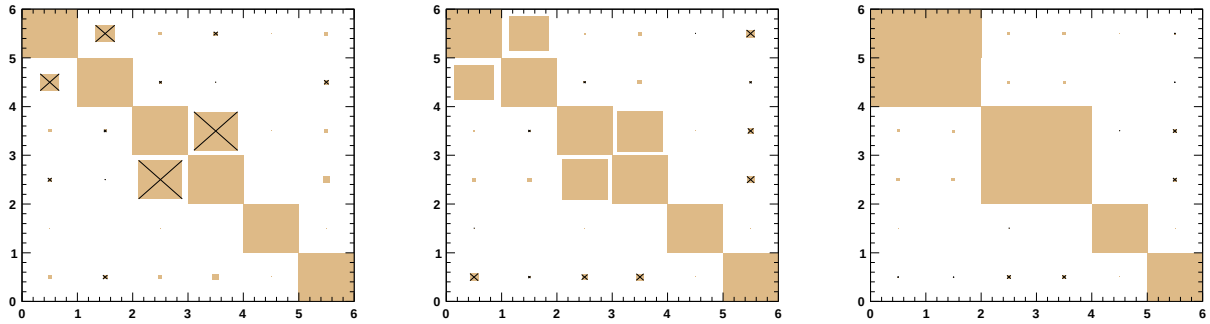

(a) Equation 70, monitor 1 is placed right after the first degrader.

(b) Equation 71, monitor 2 is placed after the quadrupole triplet, before the second degrader.

(c) Equation 72 monitor 3 is placed after the second degrader.

Figure 19: The correlation matrices at three different positions, captured with monitors along the beam line, are visualized. The correlation values range from -1 to 1, with ones on the diagonal per definition. The squares correspond in size to the value and have a cross if the sign is negative. The x- and y-axis range from 1 to 6 to relate directly to the 6 dimensional correlation matrix B. This means the square on the left corner at top stands for δ_{xx}, whereas the square on the right bottom represents $\delta_{p_z p_z}$.

5.4.1. Output emittance

In order to estimate the final emittance, a fourth monitor is installed at 3.0 m, assuming further optical elements to subsequently shape the beam for proton therapy will be placed there. The beam distribution captured at 3.0 m has the form

$$\begin{aligned}
\sigma_x^{\text{beam}} &= \begin{pmatrix} 494.6 \pm 10.49 \text{ mm}^2 & 871.5 \pm 5.158 \text{ mm mrad} \\ 871.5 \pm 5.158 \text{ mm mrad} & 1546 \pm 5.104 \text{ mrad}^2 \end{pmatrix} \\
&= 72.18 \pm 95.12 \text{ mm mrad} \cdot \begin{pmatrix} 6.852 \pm 9.031 \text{ mm/mrad} & -12.07 \pm -15.91 \\ -12.07 \pm -15.91 & 21.42 \pm 28.23 \text{ mrad/mm} \end{pmatrix} \\
\sigma_y^{\text{beam}} &= \begin{pmatrix} 537.2 \pm 11.09 \text{ mm}^2 & 937.1 \pm 5.448 \text{ mm mrad} \\ 937.1 \pm 5.448 \text{ mm mrad} & 1641 \pm 5.369 \text{ mrad}^2 \end{pmatrix} \\
&= 58.36 \pm 131.4 \text{ mm mrad} \cdot \begin{pmatrix} 9.204 \pm 20.73 \text{ mm/mrad} & -16.06 \pm -36.16 \\ -16.06 \pm -36.16 & 28.12 \pm 63.32 \text{ mrad/mm} \end{pmatrix}
\end{aligned} \tag{59}$$

The emittance captured in this monitor thus equals:

$$\begin{aligned}
\epsilon_x^{1\sigma} &= 123.5 \pm 5.552 \text{ mm mrad} \\
\epsilon_y^{1\sigma} &= 61.52 \pm 1.289 \text{ mm mrad}
\end{aligned}$$

The emittances gathered in monitor 4 at 3.0 m are better than for the double degrader with no cut in energy.

	conventional degrader	double degrader	reduction in emittance
x-direction	$\epsilon_x^{1\sigma} = 102.5 \pm 2.826$ mm mrad	$\epsilon_x^{1\sigma} = 123.5 \pm 5.552$ mm mrad	-20.5 %
y-direction	$\epsilon_y^{1\sigma} = 103.5 \pm 3.351$ mm mrad	$\epsilon_y^{1\sigma} = 61.52 \pm 1.289$ mm mrad	40.6 %

Compared to the output emittance of a conventional degrader, the output emittance of the double degrader experiences a reduction of about a factor $\sim \frac{1}{120.5\ \%} \cdot \frac{1}{59.4\ \%} = \mathbf{1.40}$. Moreover, already in the

triplet (section 5.2) the emittance values in x-direction ϵ_x are growing. This is not expected to happen as in linear optics the quadrupole should conserve the beam emittance.

5.4.2. Emittance growth

Dr. Klaus Floettmann did research on beam emittance features and different definitions of the emittance in current use for tracking simulations [Flo03]. He pointed out the influence of a distribution in energy on changes in beam emittance as well as discrepancies between local and non-local emittance values. Local emittance values are rms emittance values measured at a specific longitudinal position. Non-local emittance values are rms emittance values measured at a certain time, hence with different longitudinal positions. In [Flo03] there are some discrepancies between local and non-local emittance values shown for a quadrupole (figure 20). This is of particular interest for our double degrader installation as it can give further insight on the emittance growth found in section 5.2, 5.3 and 5.4.

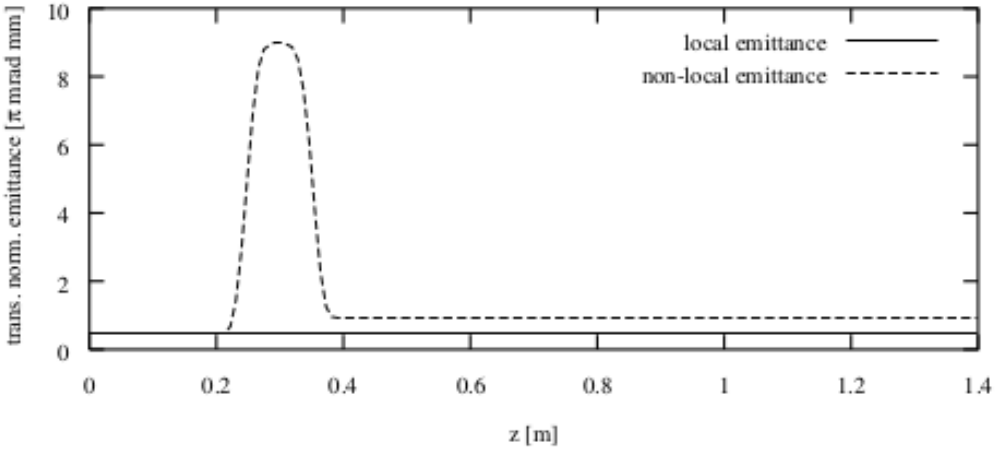

Figure 20: Development of the local and non-local emittance in a beam line with a quadrupole placed at $z = 0.3$ m estimated by [Flo03].

[Flo03] leads the growth in emittance back to large correlation values found for the non-local emittance:

" The latter procedure [non-local emittance estimation] introduces obviously large correlated emittance contributions, for example, when the emittance is calculated inside a beam line element where the head of the bunch has integrated over fields which the tail has not yet seen.' [Flo03, p.6].

To reproduce such a result and investigate dependencies of the emittance growth on the initial beam distribution, I have written a `MATLAB` routine to track particles through a quadrupole triplet similar as in `OPAL`.

The tracking implemented in `MATLAB` initially was based on the hard-edge model. This means that, from the moment on a particle enters a quadrupole, it experiences a strong magnetic field. Doing a leap-frog integration, the magnetic field rises within one step from zero (last step in front of the quadrupole) to its full strength (first step inside the quadrupole). When treating non-linearities, the first approximation to do is adding fringe fields to optical elements with magnetic fields. In the `MATLAB` simulations shown in figure 21, the results from simulations with and without fringe fields are shown. As can be seen in figure 21, the simulation with fringe fields for each quadrupole (figure 21a) is smoother than the simulation with the hard-edge model (figure 21b). Furthermore, the discrepancies between the local and non-local emittance values become smaller for the model with the fringe field. This is in favour of the model with fringe fields. Comparing figure 21a to figure 21d it becomes evident, that the initial beam distribution values σ_x and σ_{p_x} have an influence on the development of the emittance values.

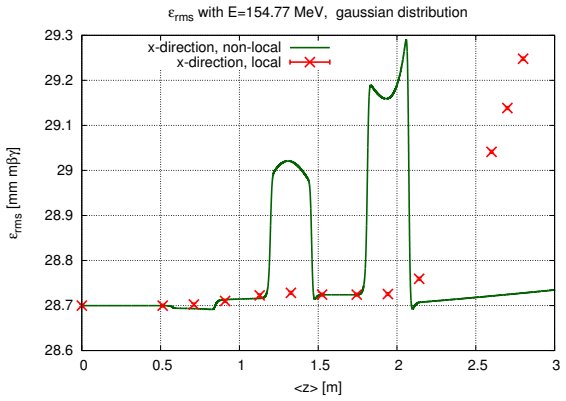

(a) The sigma matrix corresponds to the beam distribution found after the first degrader element in the double degrader installation of section 5.4: $\sigma_x = 1.92 \cdot 10^{-3}$ m, $\sigma_{p_x} = 15.192 \cdot 10^{-3} \beta\gamma$. This tracking simulation includes fringe fields for each quadrupole.

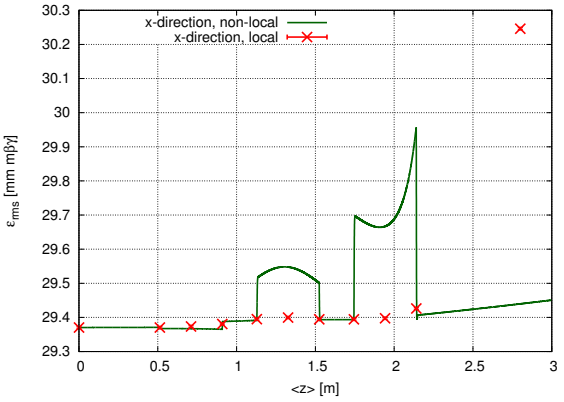

(b) The sigma matrix corresponds to the one found after the first degrader element in the double degrader installation of section 5.4: $\sigma_x = 1.92 \cdot 10^{-3}$ m, $\sigma_{p_x} = 15.192 \cdot 10^{-3} \beta\gamma$. This tracking simulation is based on the hard-edge model.

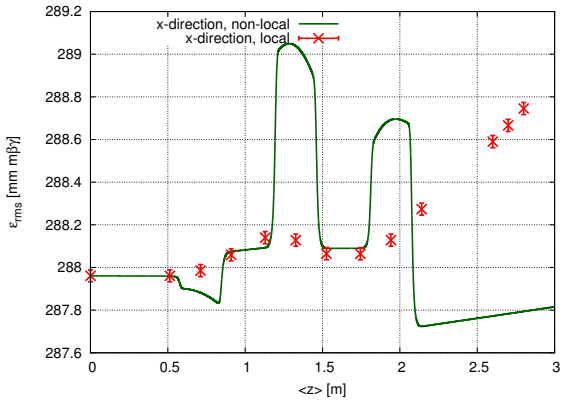

(c) $\sigma_x = 19.2 \cdot 10^{-3}$ m, $\sigma_{p_x} = 15.192 \cdot 10^{-3} \beta\gamma$. This tracking simulation includes fringe fields for each quadrupole.

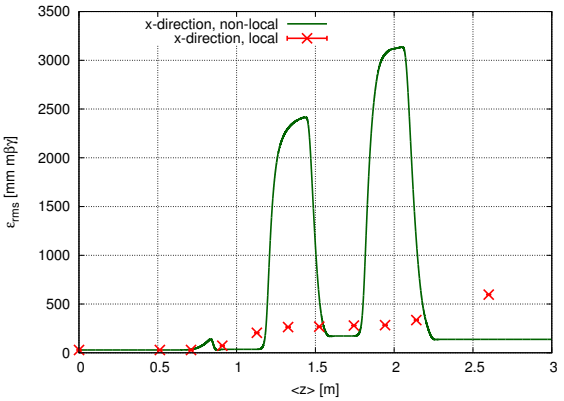

(d) $\sigma_x = 0.192 \cdot 10^{-3}$ m, $\sigma_{p_x} = 151.92 \cdot 10^{-3} \beta\gamma$. This tracking simulation includes fringe fields for each quadrupole.

Figure 21: Different tracking simulations from a `MATLAB` routine. They show different behaviour of local and non-local emittance values in dependence on input distribution values. All simulations are performed with a kinetic energy of exactly 154.77 MeV and 10^5 protons.

Roughly, the local and non-local emittance values seem to behave as proposed by [Flo03]. The local emittance values approximately stay constant when the beam travels the quadrupole triplet and the non-local emittance values fluctuate heavily. However, the three local emittance values ranging from $z = 2.5$ m to $z = 3.0$ m do not stay close to the initial beam emittance value, but grow steadily.

Insights found with the tracking simulations in time implemented in `MATLAB` are

- Hard-Edge model of a quadrupole is less accurate than the model with fringe fields. This suggests to treat the double degrader simulations in `OPAL` not purely linear but with respect to fringe fields.
- the larger the σ_x, σ_{p_x} values, the larger the discrepancies between local- and non-local emittance values become.
- neither non-local nor local emittance values do stay constant when the beam travels a quadrupole triplet

6. Comparison

6.1. Comparison to Dr. Pedroni's results

In a PSI-internal report, Dr. Pedroni guessed the rate of inelastic proton scattering to be about $\sim 30\%$ [Ped12b, p.2]. With the help of `FLUKA` and `OPAL`, it was possible to make a new guess (see section 4.3.2). Comparisons of `FLUKA` simulations with `OPAL` simulations, both simulating an equivalent degrader, deliver a rate of $\sim 4.5\%$ protons, amongst all scattering actions, leaving a degrader with an energy below the average energy. Furthermore, the number of particles leaving the degrader at the desired energy found with `FLUKA` overlap well with the number of particles at the same energy simulated with `OPAL`. On top of this, the cut in energy applied on the double degrader in section 5.4 excludes all protons at undesired energies. This leaves only protons from the `OPAL` simulation, which agree well with the `FLUKA` simulations. Consequently, inelastic scattering accounts only for a small part in the final double degrader installation.

Dr. Pedroni found a reduction in emittance of about a factor 3.48. This factor is much higher than the one found with `OPAL`. Nevertheless, the decrease in emittance found with `OPAL` is expected to be smaller, as the boundary conditions differ. Dr. Pedroni assumed a higher density $\rho = 2.26\ \mathrm{g/cm^3}$ and ignored chromatic effects. In the `OPAL` simulations, the cut in energy was necessary to avoid chromatic aberrations. Finally, the more realistic graphite density $\rho = 1.88\ \mathrm{g/cm^3}$ automatically induces a larger radiation length, resulting in a higher beam spread. The higher the beam spread after the first degrader is, the more difficult the refocusing on the second degrader becomes. Summing up, the more realistic boundaries used in the `OPAL` simulations naturally deliver a worse reduction in emittance.

6.2. Comparison to Dr. Baumgarten's results

Dr. Baumgarten's quadrupole triplet causes a standard deviation of maximally $\sim 7,5$ cm. The aperture of the quadrupole guiding this beam, needs to let pass at least 2.5σ. Hence, the minimum aperture of this quadrupole is $2 \cdot 2,5 \cdot 7,5\ \mathrm{cm} = 37,5\ \mathrm{cm}$. Dr. Baumgarten consequently estimated the required pole tip field to be $2 \cdot 2,5 \cdot 1.22\ \mathrm{T} = 6,1\ \mathrm{T}$. This field is too high to be reached by a warm magnet, but achievable with superconducting magnets. As superconducting magnets are inappropriate for medical proton therapy, Dr. Baumgarten dismissed this quadrupole as valuable for a double degrader installation (see report [Bau13]).
The quadrupole triplet found in this work differs slightly from Dr. Baumgarten's triplet. The standard deviation is maximally ~ 5.6 cm, provoking an aperture of at least $2 \cdot 2,5 \cdot 5.6\ \mathrm{cm} = 28\ \mathrm{cm}$ and a pole tip field of $0.28\ \mathrm{m} \cdot 15.008\ \mathrm{T/m} = 4.2022\ \mathrm{T}$. The results, pre calculated with `MADX` and slightly altered by `OPAL`, differ from Dr. Baumgarten's results as the double degrader installation incorporates other boundaries. The minimal distance between the first degrader and the first quadrupole element is chosen to be 30 cm, whereas Dr. Baumgarten chose 50 cm.

	[Bau13]	Master thesis
minimum separation between the degrader and the quadrupole:	50 cm	30 cm
maximum 1σ beam size	$\sigma_{\max} = 7,5$ cm	$\sigma_{\max} = 5,6$ cm
aperture of second quadrupole	37,5 cm	28 cm
maximum pole tip field	$B = 6,1$ T	$B = 4,2$ T

Table 5: Dr. Baumgarten's results in relation to the quadrupole triplet needed for the double degrader installation, are compared to the quadrupole triplet found with `OPAL`. Dr. Baumgarten dismissed his triplet as inaccessible for proton therapy. The degrader demonstrated in this paper is slightly better but still not suitable for proton therapy.

7. Conclusion

The decrease in emittance could be approved by simulating a double degrader with OPAL. By the usage of a double degrader, the emittance can be decreased about a factor 1.40, when compared with the emittance emerging from a conventional degrader. This is neither as high as the decrease factor Dr. Farley estimated, nor does it achieve the decrease factor Dr. Pedroni found:

Dr. Farley	:	decrease factor	=	4
Dr. Pedroni	:	decrease factor	=	3.48
OPAL-simulations	:	decrease factor	=	1.40

However, the reduction in emittance was not expected to be as large as the ones Dr. Farley and Dr. Pedroni estimated, due to the application of more realistic boundary conditions. Moreover, the need of superconducting magnets for correct focusing is a disillusionment. As Dr. Baumgarten pointed out, this limits the usage of the double degrader for medical purposes for the time being. Nevertheless, the mathematically derived loss in beam emittance is successfully tested with OPAL simulations. Additionally, OPAL makes use of the same scattering physics but different implementation (section 4.1.2) than Dr. Farley did (section 2.1.1). Hence, approaching the subject of the double degrader from a different point of view still delivers a decrease in emittance.

Outlook

If the emittance in x decreased similarly as the emittance in y does, a total reduction in emittance of about a factor $\left(\frac{1}{0.594}\right)^2 \approx \mathbf{2.8}$ could be expected. This high factor and a deeper understanding of the emittance estimation for tracking simulations make it worth to have e closer look on the growing rms emittance values found in the quadrupole triplet in section 5.2.

Acknowledgements

First and foremost, I thank Dr. Andreas Adelmann. You guided me through bigger as well as smaller problems with great patience and humour. Furthermore, I thank Dr. Daniela Kiselev for the FLUKA crash course and discussions about the implementation of scattering physics in OPAL. Also, I thank Dr. Christian Baumgarten for several encouraging conversations about quadrupole triplets and the cyclotron COMET. Additionally, Dr. Baumgarten provided me his Runge-Kutta integration program for helpful comparisons. Last but not least, many thanks to Achim Gsell, Anna Kolano, Dr. Tülin Kaman, Carina Stritt and Nadine Engbersen for their help with technical problems, discussions about physics, spell-checking and supportive, problem-oriented conversations.

A. Conversions between MADX and OPAL

Gaussian Distribution and Twiss Parameters in OPAL and MADX

$$\sigma_{beam} = \begin{pmatrix} \sigma_x & \sigma_{xp_x} \\ \sigma_{xp_x} & \sigma_{p_x} \end{pmatrix} = \begin{pmatrix} \sigma_x & \delta\cdot\sqrt{\sigma_x\sigma_{p_x}} \\ \delta\cdot\sqrt{\sigma_x\sigma_{p_x}} & \sigma_{p_x} \end{pmatrix} = \begin{pmatrix} < x^2 > & < xp_x > \\ < xp_x > & < p_x^2 > \end{pmatrix} = \begin{pmatrix} \frac{1}{N}\sum_{i=1}^{N} x_i^2 & \frac{1}{N}\sum_{i=1}^{N} x_i p_{x_i} \\ \frac{1}{N}\sum_{i=1}^{N} x_i p_{x_i} & \frac{1}{N}\sum_{i=1}^{N} p_{x_i}^2 \end{pmatrix} = \epsilon\cdot\begin{pmatrix} \beta_T & -\alpha_T \\ -\alpha_T & \gamma_T \end{pmatrix}$$

$$\begin{aligned} \bar{p}_x &= \sqrt{\frac{1}{N}\sum_{i=1}^{N} p_{x_i}^2} &&= \sqrt{\sigma_{p_x}} & \bar{x} &= \sqrt{\frac{1}{N}\sum_{i=1}^{N} x_i^2} \\ \bar{p}_y &= \sqrt{\frac{1}{N}\sum_{i=1}^{N} p_{y_i}^2} &&= \sqrt{\sigma_{p_y}} & \bar{y} &= \sqrt{\frac{1}{N}\sum_{i=1}^{N} y_i^2} \end{aligned}$$

$$\begin{aligned} \gamma &= \frac{E_{kin}+m_p}{m_p} & \beta &= \sqrt{1-\frac{1}{\gamma^2}} = \frac{v}{c} \\ (\beta\gamma) &= \frac{E_{kin}+m_p}{m_p}\cdot\sqrt{1-\frac{1}{\gamma^2}} = \frac{\beta}{\sqrt{1-\beta^2}} & \mathrm{B}\rho &= \frac{(\beta\gamma)\cdot m_p\cdot 10^9}{c}\ [\mathrm{T\ m}] \\ m_p &= 0.939277\ [\mathrm{GeV}] & c &= 299792458\ [\mathrm{m/s}] \end{aligned}$$

Quantity	MADX		Conversion			OPAL-Output	
Momenta	$\bar{p}_x$	[rad]	$\bar{p}_x\,[\beta\gamma]$	=	$(\bar{p}_x\,[\mathrm{rad}])\cdot(\beta\gamma)$	$\bar{p}_x$	$[\beta\gamma]$
Correlation of $\bar{x}$,$\bar{p}_x$	δ	[1]	δ	=	$(\sigma_{xp_x}\,[\mathrm{m\ rad}])\,/\,((\bar{p}_x\,[\mathrm{rad}])\cdot(\bar{x}\,[\mathrm{m}]))$	δ	[1]
				=	$(\sigma_{xp_x}\,[\mathrm{m\ rad}])\,/\sqrt{(\sigma_x\,[\mathrm{m}^2])\cdot(\sigma_{p_x}\,[\mathrm{rad}^2])}$		
Emittance	ϵ_x	[m rad]	$\epsilon_x[\mathrm{m}\ \beta\gamma]$	=	$\sqrt{(\bar{p}_x\,[\beta\gamma])^2\cdot(\bar{x}\,[\mathrm{m}])^2-(\delta\cdot(\bar{x}\,[\mathrm{m}])\cdot(\bar{p}_x\,[\beta\gamma]))^2}$	ϵ_x	[m $\beta\gamma$]
				=	$\sqrt{\left(\sigma_{p_x}\left[(\beta\gamma)^2\right]\right)\cdot(\sigma_x\,[\mathrm{m}^2])-\left(\delta\cdot\sqrt{(\sigma_x\,[\mathrm{m}^2])\cdot\left(\sigma_{p_x}\left[(\beta\gamma)^2\right]\right)}\right)^2}$		
				=	$\sqrt{\left(\sigma_{p_x}\left[(\beta\gamma)^2\right]\right)\cdot(\sigma_x\,[\mathrm{m}^2])-(\sigma_{xp_x}\,[\mathrm{m\ }\beta\gamma])^2}$		
Twiss Parameter α_T	α_T	[1]	α_T [1]	=	$-\delta\cdot(\bar{x}\,[\mathrm{m}])\cdot(\bar{p}_x\,[\beta\gamma])\,/\,(\epsilon_x[\mathrm{m}\ \beta\gamma])$	α_T	[1]
				=	$-\delta\cdot\sqrt{(\sigma_x\,[\mathrm{m}^2])\cdot\left(\sigma_{p_x}\left[(\beta\gamma)^2\right]\right)}\,/\,(\epsilon_x[\mathrm{m}\ \beta\gamma])$		
Twiss Parameter β_T	β_T	[m/rad]	$\beta_T\,[\mathrm{m}/\beta\gamma]$	=	$(\bar{x}\,[\mathrm{m}])^2/(\epsilon_x[\mathrm{m}\ \beta\gamma])$	β_T	[m/$\beta\gamma$]
				=	$(\sigma_x\,[\mathrm{m}^2])\,/\,(\epsilon_x[\mathrm{m}\ \beta\gamma])$		
Twiss Parameter γ_T	γ_T	[rad/m]	$\gamma_T\,[\beta\gamma/\mathrm{m}]$	=	$(\bar{p}_x\,[\beta\gamma])^2/(\epsilon_x[\mathrm{m}\ \beta\gamma])$	γ_T	[$\beta\gamma$/m]
				=	$\left(\sigma_{p_x}\left[(\beta\gamma)^2\right]\right)/(\epsilon_x[\mathrm{m}\ \beta\gamma])$		
Focusing strength	k_1	[m^{-2}]	$k_1\,[\mathrm{T/m}]$	=	$(k_1\,[\mathrm{m}^{-2}])\cdot(\mathrm{B}\rho\,[\mathrm{T\ m}])$	k_1	[T/m]
Quantity	MADX		Conversion			OPAL-Input	
Element Position	at := Center of the element	[m]	ELEMEDGE	=	(Center of the element) - (Length of the element)/2	ELEMEDGE = Begin of the element	[m]
Quantity	OPAL-Output		Conversion			OPAL-Input	
Momenta	$\bar{p}_x$	$[\beta\gamma]$	p_x [eV]	=	$m_p\cdot 10^9\cdot\left(\sqrt{(\bar{p}_x\,[\beta\gamma])^2+1}-1\right)$	$\bar{p}_x$	[eV]

Figure 22: Cheat sheet written to look up unit-conversions between the tools MADX, OPAL and TRANSPORT.

B. Treatment of experimental data

There are several ways to describe the proton distribution and confusingly many notations of the emittance. The conventions used in this report, are written down in this section.
The beam distribution is assumed to be a Gaussian, where the x-, y- and z-plane are assumed to be decoupled from each other. The covariance matrix, describing the proton distribution, has the following form:

$$\sigma^{\text{beam}} = \begin{pmatrix} \sigma_{xx} & \sigma_{xp_x} & \sigma_{xy} & \sigma_{xp_y} & \sigma_{xz} & \sigma_{xp_z} \\ \sigma_{xp_x} & \sigma_{p_xp_x} & \sigma_{yp_x} & \sigma_{p_xp_y} & \sigma_{zp_x} & \sigma_{p_xp_z} \\ \sigma_{xy} & \sigma_{yp_x} & \sigma_{yy} & \sigma_{yp_y} & \sigma_{yz} & \sigma_{yp_z} \\ \sigma_{xp_y} & \sigma_{p_xp_y} & \sigma_{yp_y} & \sigma_{p_yp_y} & \sigma_{zp_y} & \sigma_{p_yp_z} \\ \sigma_{xz} & \sigma_{zp_x} & \sigma_{yz} & \sigma_{zp_y} & \sigma_{zz} & \sigma_{zp_z} \\ \sigma_{xp_z} & \sigma_{p_xp_z} & \sigma_{yp_z} & \sigma_{p_yp_z} & \sigma_{zp_z} & \sigma_{p_zp_z} \end{pmatrix}. \tag{60}$$

The Gaussian of the x, p_x-plane looks like

$$f(x,p_x) = \frac{1}{2\pi\sqrt{\sigma_{xx}\sigma_{p_xp_x}\left(1-\delta_{xp_x}^2\right)}} \cdot \exp\left(\frac{-1}{2\left(1-\delta_{xp_x}^2\right)} \cdot \left[\frac{\left(x-\bar{x}\right)^2}{\sigma_{xx}} + \frac{\left(p_x-\bar{p}_x\right)^2}{\sigma_{p_xp_x}} - \frac{2\delta_{xp_x}\left(x-\bar{x}\right)\left(p_x-\bar{p}_x\right)}{\sqrt{\sigma_{xx}\sigma_{p_xp_x}}}\right]\right).$$

The Gaussian of the y- respectively the z-plane are analogous. The mean values $\bar{x}$, $\bar{p}_x$, $\bar{y}$ and $\bar{p}_y$ are approximately zero, which results from the definition of the coordinate system. The protons are assumed to be placed initially around the coordinates $(x, p_x, y, p_y, z, p_z) = (0,0,0,0,0,0)$ and travel along the z-coordinate through the optical elements such as degrader and quadrupole. The mean value in x and y stays zero, with variations due to statistical fluctuations. The square root of the standard deviation describes the beam radius in each direction. Furthermore, the correlation value δ_{xp_x}, ranging from -1 to 1, shows how strongly the x- and y-values are linearly coupled to each other. The closer δ_{xp_x} to one is, the closer the x- and y values are aligned on a linear slope, whose gradient has the same sign as δ_{xp_x}.

$$\bar{x} = \frac{1}{N}\sum_{i=1}^{N} x_i \qquad \bar{y} = \frac{1}{N}\sum_{i=1}^{N} y_i \tag{61}$$

$$\bar{p}_x = \frac{1}{N}\sum_{i=1}^{N} p_{x_i} \qquad \bar{p}_y = \frac{1}{N}\sum_{i=1}^{N} p_{y_i} \tag{62}$$

$$\sigma_{xx} = \frac{1}{N}\cdot\sum_{i=1}^{N}\left(x_i-\bar{x}\right)^2 \qquad \sigma_{yy} = \frac{1}{N}\cdot\sum_{i=1}^{N}\left(y_i-\bar{y}\right)^2 \tag{63}$$

$$\sigma_{p_xp_x} = \frac{1}{N}\cdot\sum_{i=1}^{N}\left(p_{x_i}-\bar{p}_x\right)^2 \qquad \sigma_{p_yp_y} = \frac{1}{N}\cdot\sum_{i=1}^{N}\left(p_{y_i}-\bar{p}_y\right)^2 \tag{64}$$

$$\delta_{x,p_x} = \frac{\sigma_{xp_x}}{\sqrt{\sigma_{xx}\sigma_{p_xp_x}}} \qquad \delta_{yp_y} = \frac{\sigma_{yp_y}}{\sqrt{\sigma_{yy}\sigma_{p_yp_y}}} \tag{65}$$

$$\sigma_{ab} = \frac{1}{N}\cdot\sum_{i=1}^{N}\left(a_i-\bar{a}\right)\left(b_i-\bar{b}\right) \tag{66}$$

$$\delta_{a,b} = \frac{\sigma_{ab}}{\sqrt{\sigma_{aa}\sigma_{bb}}} \qquad \forall\ a,b = x,y,z,p_x,p_y,p_z \tag{67}$$

The formulas listed here can be looked up in [WBM+09]. If the assumption of decoupled planes holds, then the six dimensional Gaussian takes the form

$$f(x, p_x, y, p_y, z, p_z) = f(x, p_x) \cdot f(y, p_y) \cdot f(z, p_z). \tag{68}$$

Additionally, the correlation matrix reduces to

$$\delta^{\text{beam}} = \begin{pmatrix} \delta_{xx} & \delta_{xp_x} & \delta_{xy} & \delta_{xp_y} & \delta_{xz} & \delta_{xp_z} \\ \delta_{xp_x} & \delta_{p_xp_x} & \delta_{yp_x} & \delta_{p_xp_y} & \delta_{zp_x} & \delta_{p_xp_z} \\ \delta_{xy} & \delta_{yp_x} & \delta_{yy} & \delta_{yp_y} & \delta_{yz} & \delta_{yp_z} \\ \delta_{xp_y} & \delta_{p_xp_y} & \delta_{yp_y} & \delta_{p_yp_y} & \delta_{zp_y} & \delta_{p_yp_z} \\ \delta_{xz} & \delta_{zp_x} & \delta_{yz} & \delta_{zp_y} & \delta_{zz} & \delta_{zp_z} \\ \delta_{xp_z} & \delta_{p_xp_z} & \delta_{yp_z} & \delta_{p_yp_z} & \delta_{zp_z} & \delta_{p_zp_z} \end{pmatrix} \approx \begin{pmatrix} 1 & \delta_{xp_x} & 0 & 0 & 0 & 0 \\ \delta_{xp_x} & 1 & 0 & 0 & 0 & 0 \\ 0 & 0 & 1 & \delta_{yp_y} & 0 & 0 \\ 0 & 0 & \delta_{yp_y} & 1 & 0 & 0 \\ 0 & 0 & 0 & 0 & 1 & \delta_{zp_z} \\ 0 & 0 & 0 & 0 & \delta_{zp_z} & 1 \end{pmatrix}, \tag{69}$$

as correlation values still contain a statistical error. To check on this assumption, the correlation matrix is calculated at multiple positions in the beam line of the double degrader. The double degrader's installation is explained in greater detail in section 5.2 and the OPAL-simulations, concerning the double degrader, are presented in section 5. With the reference to those upcoming sections, some correlation matrices are anticipated and shown here to confirm the validity of decoupled planes. Three positions along the beam line are particularly interesting: after the first degrader, before the second degrader and after the second degrader. At each of those places, the OPAL-simulation contains a monitor. Whenever OPAL tracks the protons through the beam line, it dumps the particles phase space coordinates (x, p_x, y, p_y, z, p_z) in a file. This data collection is suitable when looking at the beam evolution in time. However, when the beam matrix at a certain coordinate z is of interest, a monitor needs to be placed there. Differently to the time oriented dumping, a monitor saves the particles phase space coordinates only when they pass through the requested room coordinate z. The monitors placement can be seen in figure 23. The protons phase space coordinates at these monitors are used to calculate the six dimensional correlation matrix, according to the formulas 61 - 67.

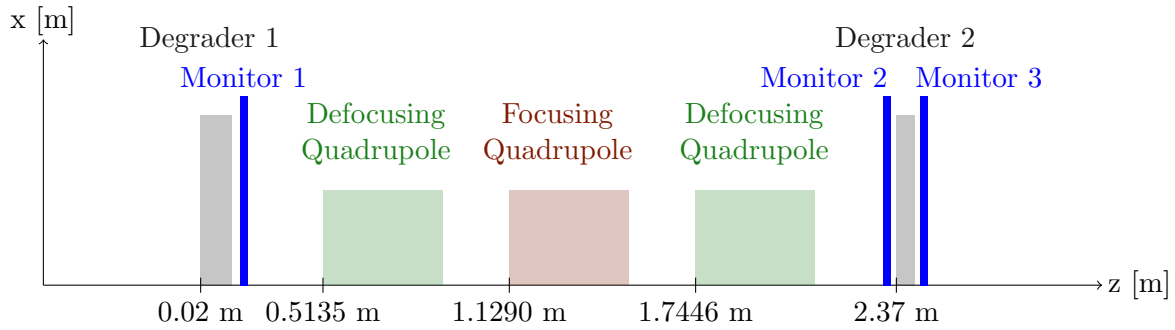

Figure 23: Double degrader installation with monitors to record the proton's phase space coordinates right after the first and second degrader, as well as before the second degrader.

The values of the correlation matrices are close to one for correlations between (x, p_x), (y, p_y) and (z, pz), but nearly zero elsewhere:

$$\delta^{\text{beam}}_{\text{monitor 1}} = \begin{pmatrix} 1 & 0,726 & -0,00394 & -0,00437 & -1,49 \cdot 10^{-19} & -0,0276 \\ 0,726 & 1 & -0,00325 & -0,00345 & 0 & -0,0157 \\ -0,00394 & -0,00325 & 1 & 0,711 & 6,91 \cdot 10^{-17} & -0,032 \\ -0,00437 & -0,00345 & 0,711 & 1 & 0 & -0,0231 \\ -1,49 \cdot 10^{-19} & 0 & 6,91 \cdot 10^{-17} & 0 & 1 & 2,69 \cdot 10^{-13} \\ -0,0276 & -0,0157 & -0,032 & -0,0231 & 2,69 \cdot 10^{-13} & 1 \end{pmatrix} \tag{70}$$

$$\delta^{\text{beam}}_{\text{monitor 2}} = \begin{pmatrix} 1 & 0,349 & -0,00775 & -0,00418 & 9,48\cdot 10^{-18} & -0,162 \\ 0,349 & 1 & -0,00266 & -0,00312 & 0 & -0,0526 \\ -0,00775 & -0,00266 & 1 & -0,579 & -5,19\cdot 10^{-17} 0,0097 & \\ -0,00418 & -0,00312 & -0,579 & 1 & 0 & -0,000529 \\ 9,48\cdot 10^{-18} & 0 & -5,19\cdot 10^{-17} & 0 & 1 & 3,59\cdot 10^{-13} \\ -0,162 & -0,0526 & 0,0097 & -0,000529 & 3,59\cdot 10^{-13} 1 & \end{pmatrix} \tag{71}$$

$$\delta^{\text{beam}}_{\text{monitor 3}} = \begin{pmatrix} 1 & 0,453 & -0,00255 & -0,00211 & 4,76\cdot 10^{-18} & -0,00745 \\ 0,453 & 1 & -0,00257 & -0,00282 & 0 & 0,00134 \\ -0,00255 & -0,00257 & 1 & 0,646 & 1,31\cdot 10^{-17} & 9,31\cdot 10^{-05} \\ -0,00211 & -0,00282 & 0,646 & 1 & 0 & -0,00298 \\ 4,76\cdot 10^{-18} & 0 & 1,31\cdot 10^{-17} & 0 & 1 & 4,24\cdot 10^{-13} \\ -0,00745 & 0,00134 & 9,31\cdot 10^{-05} & -0,00298 & 4,24\cdot 10^{-13} & 1 \end{pmatrix} \tag{72}$$

These correlation matrices belong to a beam of 10^5 protons, entering the double degrader drawn in figure 23 with an energy of 250 MeV. Furthermore, the beam distribution values entered into this double degrader are taken from the output delivered by the cyclotron COMET. Surprisingly, the correlation matrix from the second monitor has the correlation values $\delta_{xp_z} = -0,162$ and $\delta_{p_x,p_z} = -0,0526$. Those values should be close to zero, but are not. Presumably, the quadrupole triplet does not focus the beam as good as intended, resulting in higher correlation values. These may be caused by the energy deviation from the first degradation process. The quadrupole triplet is designed for protons at exactly 154.77 MeV, hence the focusing for particles with a kinetic energy differing from 154.77 MeV is imprecise. This difficulty is treated in more detail in section 5.

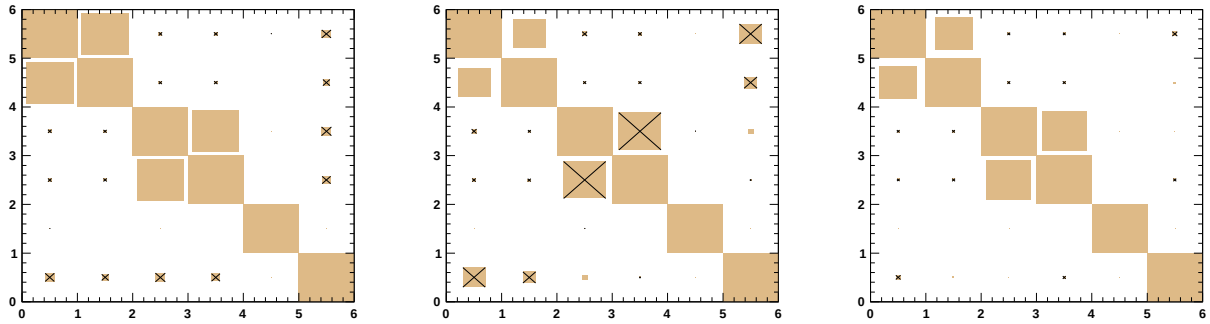

(a) Equation 70, monitor 1 is placed right after the first degrader.

(b) Equation 71, monitor 2 is placed after the quadrupole triplet, before the second degrader.

(c) Equation 72 monitor 3 is placed after the second degrader.

Figure 24: The correlation matrices at three different positions, captured with monitors along the beam line, are visualized. The correlation values range from -1 to 1, with ones on the diagonal per definition. The squares correspond in size to the correlation value and have a cross if the correlation's sign is negative. The x- and y-axis range from 1 to 6 to relate directly to the 6 dimensional correlation matrix, written down in equation B. Accordingly, the square on the left corner at top stands for δ_{xx}, whereas the square on the right bottom represents $\delta_{p_z p_z}$.

B.1. Emittance

The definition of the emittance used in this report, is the rms emittance, listed in table 6. In proton accelerator physics, the $\epsilon^{4\sigma}$ is of importance, as it covers 99.994 percent of all the protons contained in the beam.

name	formula	ratio of beam covered
rms emittance	$\epsilon_x^{1\sigma} = \sqrt{\sigma_{xx}\sigma_{p_xp_x} - \sigma_{xp_x}^2}$	68.269 %
2 rms emittance	$\epsilon_x^{2\sigma} = 4 \cdot \sqrt{\sigma_{xx}\sigma_{p_xp_x} - \sigma_{xp_x}^2} = 4 \cdot \epsilon^{1\sigma}$	95.450 %
3 rms emittance	$\epsilon_x^{3\sigma} = 9 \cdot \epsilon_x^{1\sigma}$	99.730 %
4 rms emittance	$\epsilon_x^{4\sigma} = 16 \cdot \epsilon_x^{1\sigma}$	99.994 %

Table 6: The rms emittance listed here refer to a two dimensional plane in the six dimensional phase space. Everything that is listed here for the x-plane works analogous in the y- and z-plane.

The emittance times π is equal to the area covered by the particles. The unit of the emittance in literature sometimes is set to π mm mrad, to indicate that the emittance times π is equal to the area. However, in this report we stick to

$$\frac{\text{Area}\,[\,\text{mm mrad}\,]}{\pi} = \epsilon\,[\,\text{mm mrad}\,]\,. \tag{73}$$

B.1.1. Error of the standard deviation

In order to focus correctly in the following section, it is important to estimate the beam radius in spatial and momenta radii. Considering that we treat the beam distribution as a Gaussian, those radii are equal to the standard deviation of the Gaussian. Hence, the error of the standard deviation needs to be calculated. This is done, with error propagation

$$\begin{aligned}
\Delta\sigma_x &= \left[\sum_{i=1}^{N}\left(\frac{\partial}{\partial x_i}(\sigma_x)\cdot\Delta x_i\right)^2\right]^{0.5} \\
&= \left[\sum_{i=1}^{N}\left(\frac{\partial}{\partial x_i}\left(\left[\frac{1}{N}\sum_{j=1}^{N}(x_j-\bar{x})^2\right]^{0.5}\right)\cdot\Delta x_i\right)^2\right]^{0.5} \\
&= \left[\sum_{i=1}^{N}\left(\frac{1}{2\cdot\left[\frac{1}{N}\cdot\sum\limits_{j=10}^{N}(x_j-\bar{x})^2\right]^{0.5}}\cdot\frac{1}{N}\cdot 2\cdot(x_i-\bar{x})\cdot\Delta x_i\right)^2\right]^{0.5} \\
&= \left[\sum_{i=1}^{N}\left(\frac{1}{N}\cdot\frac{1}{\sigma_x}\cdot(x_i-\bar{x})^2\right)^2\right]^{0.5} = \frac{1}{\sigma_x}\cdot\left[\sum_{i=1}^{N}\frac{(x_i-\bar{x})^4}{N^2}\right]^{0.5}.
\end{aligned} \tag{74}$$

The error for the standard deviation of the x-momenta is calculated analogously

$$\Delta\sigma_{p_x} = \frac{1}{\sigma_{p_x}}\cdot\left[\sum_{i=1}^{N}\frac{(p_{x_i}-\bar{p_x})^4}{N^2}\right]^{0.5}. \tag{75}$$

B.1.2. Error of the rms emittance

The beam intensity is defined by the amount of particles per area per time step. Assuming constant momenta distribution, with increasing emittance, the intensity decreases and contrariwise. In order to make any statements about the beam intensity, the emittance and its error must be known. Tracking the protons through the double degrader installation and doing the calculus from the formulas in the previous section delivers the emittance. The lastly needed ingredient is the error estimation

$$
\begin{aligned}
\epsilon^2 &= \sigma_{xx}\sigma_{p_xp_x} - \sigma_{xp_x}^2 \\
\left(\Delta\epsilon^2\right)^2 &= g^{\mathrm{T}} A g \\
g^{\mathrm{T}} &= \begin{pmatrix} \frac{\partial\epsilon^2}{\partial\sigma_{xx}} & \frac{\partial\epsilon^2}{\partial\sigma_{p_xp_x}} & \frac{\partial\epsilon^2}{\partial\sigma_{xp_x}} \end{pmatrix} \\
A &= \begin{pmatrix} \mathrm{cov}\left(\sigma_{xx},\sigma_{xx}\right) & \mathrm{cov}\left(\sigma_{xx},\sigma_{p_xp_x}\right) & \mathrm{cov}\left(\sigma_{xx},\sigma_{xp_x}\right) \\ \mathrm{cov}\left(\sigma_{p_xp_x},\sigma_{xx}\right) & \mathrm{cov}\left(\sigma_{p_xp_x},\sigma_{p_xp_x}\right) & \mathrm{cov}\left(\sigma_{p_xp_x},\sigma_{xp_x}\right) \\ \mathrm{cov}\left(\sigma_{xp_x},\sigma_{xx}\right) & \mathrm{cov}\left(\sigma_{xp_x},\sigma_{p_xp_x}\right) & \mathrm{cov}\left(\sigma_{xp_x},\sigma_{xp_x}\right) \end{pmatrix}
\end{aligned}
$$

$$
\begin{aligned}
\rightarrow \left(\Delta\epsilon^2\right)^2 &= \left(\frac{\partial\epsilon^2}{\partial\sigma_{xx}}\right)^2 \mathrm{cov}\left(\sigma_{xx},\sigma_{xx}\right) + \left(\frac{\partial\epsilon^2}{\partial\sigma_{p_xp_x}}\right)^2 \mathrm{cov}\left(\sigma_{p_xp_x},\sigma_{p_xp_x}\right) + \left(\frac{\partial\epsilon^2}{\partial\sigma_{xp_x}}\right)^2 \mathrm{cov}\left(\sigma_{xp_x},\sigma_{xp_x}\right) \\
&+ 2\cdot\frac{\partial\epsilon^2}{\partial\sigma_{xx}}\frac{\partial\epsilon^2}{\partial\sigma_{p_xp_x}}\mathrm{cov}\left(\sigma_{xx},\sigma_{p_xp_x}\right) + 2\cdot\frac{\partial\epsilon^2}{\partial\sigma_{xx}}\frac{\partial\epsilon^2}{\partial\sigma_{xp_x}}\mathrm{cov}\left(\sigma_{xx},\sigma_{xp_x}\right) + 2\cdot\frac{\partial\epsilon^2}{\partial\sigma_{p_xp_x}}\frac{\partial\epsilon^2}{\partial\sigma_{xp_x}}\mathrm{cov}\left(\sigma_{p_xp_x},\sigma_{xp_x}\right) \\
&= \sigma_{p_xp_x}^2\mathrm{cov}\left(\sigma_{xx},\sigma_{xx}\right) + \sigma_{xx}^2\mathrm{cov}\left(\sigma_{p_xp_x},\sigma_{p_xp_x}\right) + 4\cdot\sigma_{xp_x}^2\mathrm{cov}\left(\sigma_{xp_x},\sigma_{xp_x}\right) \\
&+ 2\cdot\sigma_{p_xp_x}\sigma_{xx}\mathrm{cov}\left(\sigma_{xx},\sigma_{p_xp_x}\right) - 4\cdot\sigma_{xx}\sigma_{xp_x}\mathrm{cov}\left(\sigma_{p_xp_x},\sigma_{xp_x}\right) - 4\cdot\sigma_{p_xp_x}\sigma_{xp_x}\mathrm{cov}\left(\sigma_{xx},\sigma_{xp_x}\right)
\end{aligned}
$$

In order to calculate the error of the rms emittance, the covariance values seen in matrix A need to be estimated

$$
\begin{aligned}
\mathrm{cov}\left(\sigma_{xx},\sigma_{xx}\right) &= \tfrac{1}{N}\sum_{i=1}^{N}\left(\tfrac{(x_i-\bar{x})^2}{N} - \tfrac{\sigma_{xx}}{N}\right)^2 \\
&= \tfrac{1}{N}\sum_{i=1}^{N}\left[\tfrac{(x_i-\bar{x})^4}{N^2} - 2\cdot\tfrac{\sigma_{xx}}{N}\cdot\tfrac{(x_i-\bar{x})^2}{N} + \tfrac{\sigma_{xx}^2}{N^2}\right] \\
&= \sum_{i=1}^{N}\tfrac{(x_i-\bar{x})^4}{N^3} - \tfrac{\sigma_{xx}^2}{N^2}
\end{aligned}
$$

$$
\begin{aligned}
\mathrm{cov}\left(\sigma_{xp_x},\sigma_{xp_x}\right) &= \tfrac{1}{N}\sum_{i=1}^{N}\left(\tfrac{(x_i-\bar{x})\left(p_{x_i}-\bar{p}_x\right)}{N} - \tfrac{\sigma_{xp_x}}{N}\right)^2 \\
&= \tfrac{1}{N}\sum_{i=1}^{N}\left[\tfrac{(x_i-\bar{x})^2\left(p_{x_i}-\bar{p}_x\right)^2}{N^2} - 2\cdot\tfrac{\sigma_{xp_x}}{N}\cdot\tfrac{(x_i-\bar{x})\left(p_{x_i}-\bar{p}_x\right)}{N} + \tfrac{\sigma_{xp_x}^2}{N^2}\right] \\
&= \sum_{i=1}^{N}\tfrac{(x_i-\bar{x})^2\left(p_{x_i}-\bar{p}_x\right)^2}{N^3} - \tfrac{\sigma_{xp_x}^2}{N^2}
\end{aligned}
$$

$$
\begin{aligned}
\mathrm{cov}\left(\sigma_{p_xp_x},\sigma_{p_xp_x}\right) &= \tfrac{1}{N}\sum_{i=1}^{N}\left(\tfrac{\left(p_{x_i}-\bar{p}_x\right)^2}{N} - \tfrac{\sigma_{p_xp_x}}{N}\right)^2 \\
&= \tfrac{1}{N}\sum_{i=1}^{N}\left[\tfrac{\left(p_{x_i}-\bar{p}_x\right)^4}{N^2} - 2\cdot\tfrac{\sigma_{p_xp_x}}{N}\cdot\tfrac{\left(p_{x_i}-\bar{p}_x\right)^2}{N} + \tfrac{\sigma_{p_xp_x}^2}{N^2}\right] \\
&= \sum_{i=1}^{N}\tfrac{\left(p_{x_i}-\bar{p}_x\right)^4}{N^3} - \tfrac{\sigma_{p_xp_x}^2}{N^2}
\end{aligned}
$$

$$
\begin{aligned}
\mathrm{cov}\left(\sigma_{xx},\sigma_{xp_x}\right) &= \tfrac{1}{N}\sum_{i=1}^{N}\left(\tfrac{(x_i-\bar{x})^2}{N} - \tfrac{\sigma_{xx}}{N}\right)\left(\tfrac{(x_i-\bar{x})\left(p_{x_i}-\bar{p}_x\right)}{N} - \tfrac{\sigma_{xp_x}}{N}\right) \\
&= \tfrac{1}{N}\sum_{i=1}^{N}\left[\tfrac{(x_i-\bar{x})^2}{N}\cdot\tfrac{(x_i-\bar{x})\left(p_{x_i}-\bar{p}_x\right)}{N} - \tfrac{\sigma_{xx}}{N}\cdot\tfrac{(x_i-\bar{x})\left(p_{x_i}-\bar{p}_x\right)}{N} - \tfrac{\sigma_{xp_x}}{N}\cdot\tfrac{(x_i-\bar{x})^2}{N} + \tfrac{\sigma_{xx}}{N}\cdot\tfrac{\sigma_{xp_x}}{N}\right] \\
&= \sum_{i=1}^{N}\tfrac{(x_i-\bar{x})^3\left(p_{x_i}-\bar{p}_x\right)}{N^2} - \tfrac{\sigma_{xx}\cdot\sigma_{xp_x}}{N^2}
\end{aligned}
$$

$$
\begin{aligned}
\mathrm{cov}\left(\sigma_{xx},\sigma_{p_xp_x}\right) &= \tfrac{1}{N}\sum_{i=1}^{N}\left(\tfrac{(x_i-\bar{x})^2}{N} - \tfrac{\sigma_{xx}}{N}\right)\left(\tfrac{\left(p_{x_i}-\bar{p}_x\right)^2}{N} - \tfrac{\sigma_{p_xp_x}}{N}\right) \\
&= \tfrac{1}{N}\sum_{i=1}^{N}\left[\tfrac{(x_i-\bar{x})^2}{N}\cdot\tfrac{\left(p_{x_i}-\bar{p}_x\right)^2}{N} - \tfrac{\sigma_{xx}}{N}\cdot\tfrac{\left(p_{x_i}-\bar{p}_x\right)^2}{N} - \tfrac{\sigma_{p_xp_x}}{N}\cdot\tfrac{(x_i-\bar{x})^2}{N} + \tfrac{\sigma_{xx}}{N}\cdot\tfrac{\sigma_{p_xp_x}}{N}\right] \\
&= \sum_{i=1}^{N}\tfrac{(x_i-\bar{x})^2\left(p_{x_i}-\bar{p}_x\right)^2}{N^3} - \tfrac{\sigma_{xx}\sigma_{p_xp_x}}{N^2}
\end{aligned}
$$

$$\begin{aligned}
\operatorname{cov}\left(\sigma_{xp_x},\sigma_{p_xp_x}\right) &= \frac{1}{N}\sum_{i=1}^{N}\left(\frac{\left(p_{x_i}-\bar{p}_x\right)^2}{N}-\frac{\sigma_{p_xp_x}}{N}\right)\left(\frac{(x_i-\bar{x})\left(p_{x_i}-\bar{p}_x\right)}{N}-\frac{\sigma_{xp_x}}{N}\right)\\
&= \frac{1}{N}\sum_{i=1}^{N}\left[\frac{\left(p_{x_i}-\bar{p}_x\right)^2}{N}\cdot\frac{(x_i-\bar{x})\left(p_{x_i}-\bar{p}_x\right)}{N}-\frac{\sigma_{p_xp_x}}{N}\cdot\frac{(x_i-\bar{x})\left(p_{x_i}-\bar{p}_x\right)}{N}-\frac{\sigma_{xp_x}}{N}\cdot\frac{\left(p_{x_i}-\bar{p}_x\right)^2}{N}\right.\\
&\quad+\left.\frac{\sigma_{p_xp_x}}{N}\cdot\frac{\sigma_{xp_x}}{N}\right]\\
&= \sum_{i=1}^{N}\frac{(x_i-\bar{x})\left(p_{x_i}-\bar{p}_x\right)^3}{N^3}-\frac{\sigma_{p_xp_x}\sigma_{xp_x}}{N^3}.
\end{aligned}$$

Inserting the covariance values from matrix A into $\left(\Delta\epsilon^2\right)^2$ results in

$$\begin{aligned}
\rightarrow\left(\Delta\epsilon^2\right)^2 &= \sigma^2_{p_xp_x}\operatorname{cov}\left(\sigma_{xx},\sigma_{xx}\right)+\sigma^2_{xx}\operatorname{cov}\left(\sigma_{p_xp_x},\sigma_{p_xp_x}\right)+4\cdot\sigma^2_{xp_x}\operatorname{cov}\left(\sigma_{xp_x},\sigma_{xp_x}\right)\\
&\quad+2\cdot\sigma_{p_xp_x}\sigma_{xx}\operatorname{cov}\left(\sigma_{xx},\sigma_{p_xp_x}\right)-4\cdot\sigma_{xx}\sigma_{xp_x}\operatorname{cov}\left(\sigma_{p_xp_x},\sigma_{xp_x}\right)-4\cdot\sigma_{p_xp_x}\sigma_{xp_x}\operatorname{cov}\left(\sigma_{xx},\sigma_{xp_x}\right)\\
&= \sigma^2_{p_xp_x}\sum_{i=1}^{N}\frac{(x_i-\bar{x})^4}{N^3}-\frac{\sigma^2_{xx}\sigma^2_{p_xp_x}}{N^2}\\
&\quad+\sigma^2_{xx}\sum_{i=1}^{N}\frac{\left(p_{x_i}-\bar{p}_x\right)^4}{N^3}-\frac{\sigma^2_{xx}\sigma^2_{p_xp_x}}{N^2}\\
&\quad+4\cdot\sigma^2_{xp_x}\sum_{i=1}^{N}\frac{(x_i-\bar{x})^2\left(p_{x_i}-\bar{p}_x\right)^2}{N^3}-4\cdot\frac{\sigma^4_{xp_x}}{N^2}\\
&\quad+2\cdot\sigma_{p_xp_x}\sigma_{xx}\sum_{i=1}^{N}\frac{(x_i-\bar{x})^2\left(p_{x_i}-\bar{p}_x\right)^2}{N^3}-2\cdot\frac{\sigma^2_{xx}\sigma^2_{p_xp_x}}{N^2}\\
&\quad-4\cdot\sigma_{xx}\sigma_{xp_x}\sum_{i=1}^{N}\frac{(x_i-\bar{x})\left(p_{x_i}-\bar{p}_x\right)^3}{N^3}+4\cdot\frac{\sigma_{xx}\sigma_{p_xp_x}\sigma^2_{xp_x}}{N^2}\\
&\quad-4\cdot\sigma_{p_xp_x}\sigma_{xp_x}\sum_{i=1}^{N}\frac{(x_i-\bar{x})^3\left(p_{x_i}-\bar{p}_x\right)}{N^3}+4\cdot\frac{\sigma_{xx}\sigma_{p_xp_x}\cdot\sigma^2_{xp_x}}{N^2}\\
&= \sigma^2_{p_xp_x}\sum_{i=1}^{N}\frac{(x_i-\bar{x})^4}{N^3}+\sigma^2_{xx}\sum_{i=1}^{N}\frac{\left(p_{x_i}-\bar{p}_x\right)^4}{N^3}+4\cdot\sigma^2_{xp_x}\sum_{i=1}^{N}\frac{(x_i-\bar{x})^2\left(p_{x_i}-\bar{p}_x\right)^2}{N^3}\\
&\quad+2\cdot\sigma_{p_xp_x}\sigma_{xx}\sum_{i=1}^{N}\frac{(x_i-\bar{x})^2\left(p_{x_i}-\bar{p}_x\right)^2}{N^3}-4\cdot\sigma_{xx}\sigma_{xp_x}\sum_{i=1}^{N}\frac{(x_i-\bar{x})\left(p_{x_i}-\bar{p}_x\right)^3}{N^3}\\
&\quad-4\cdot\sigma_{p_xp_x}\sigma_{xp_x}\sum_{i=1}^{N}\frac{(x_i-\bar{x})^3\left(p_{x_i}-\bar{p}_x\right)}{N^3}\\
&\quad-4\cdot\frac{\sigma^2_{xx}\sigma^2_{p_xp_x}}{N^2}-4\cdot\frac{\sigma^4_{xp_x}}{N^2}+8\cdot\frac{\sigma_{xx}\sigma_{p_xp_x}\cdot\sigma^2_{xp_x}}{N^2}.
\end{aligned}$$

Finally, the error of the rms emittance needs to be estimated by error propagation using $\epsilon=\sqrt{\epsilon^2}$

$$\begin{aligned}
\Delta\epsilon &= \frac{\partial\sqrt{\epsilon^2}}{\partial\epsilon^2}\cdot\Delta\epsilon^2\\
&= \frac{1}{2\epsilon}\cdot\left[\sigma^2_{p_xp_x}\sum_{i=1}^{N}\frac{(x_i-\bar{x})^4}{N^3}+\sigma^2_{xx}\sum_{i=1}^{N}\frac{\left(p_{x_i}-\bar{p}_x\right)^4}{N^3}+4\cdot\sigma^2_{xp_x}\sum_{i=1}^{N}\frac{(x_i-\bar{x})^2\left(p_{x_i}-\bar{p}_x\right)^2}{N^3}\right.\\
&\quad+2\cdot\sigma_{p_xp_x}\sigma_{xx}\sum_{i=1}^{N}\frac{(x_i-\bar{x})^2\left(p_{x_i}-\bar{p}_x\right)^2}{N^3}-4\cdot\sigma_{xx}\sigma_{xp_x}\sum_{i=1}^{N}\frac{(x_i-\bar{x})\left(p_{x_i}-\bar{p}_x\right)^3}{N^3}\\
&\quad-4\cdot\sigma_{p_xp_x}\sigma_{xp_x}\sum_{i=1}^{N}\frac{(x_i-\bar{x})^3\left(p_{x_i}-\bar{p}_x\right)}{N^3}\\
&\quad\left.-4\cdot\frac{\sigma^2_{xx}\sigma^2_{p_xp_x}}{N^2}-4\cdot\frac{\sigma^4_{xp_x}}{N^2}+8\cdot\frac{\sigma_{xx}\sigma_{p_xp_x}\cdot\sigma^2_{xp_x}}{N^2}\right]^{0.5}.
\end{aligned}$$

C. Analysis with ROOT

All the plots containing data from OPAL simulations are plotted with ROOT. ROOT is a C++ library useful for data processing and analysing [Tea] with great tutorials (http://root.cern.ch/root/html/tutorials/). In order to read in data from the OPAL output-files in *h5*-format, the H5root-library (from the webpage http://amas.web.psi.ch/tools/H5root/index.html) is needed. It is a little bit tricky to add H5root to your libraries in use. Suppose the root-file to plot the OPAL-data is called analyze.C, then the program frame looks like:

```
#include <TFile.h>
#include <TTree.h>
#include <Riostream.h>
#include <TMath.h>
#include <TLegend.h>
#include <sstream>
#include <TF1.h>
#include <TCutG.h>
#include <TDecompChol.h>
#include <TMatrixD.h>
#include <TMatrixDLazy.h>
#include <TVectorD.h>
#include <TDecompLU.h>
#include <TDecompSVD.h>

void analyze(){

        if (TString(gSystem->GetBuildArch()) == TString("macosx64"))
                gSystem->Load("libh5root.dylib");
        else
                gSystem->Load("libh5root.so");


                ...
}
```

The figures 6, 7, 9 and 10 superpose data from FLUKA and OPAL simulations. The output from FLUKA is binned and requires the OPAL data to become binned in the same manner. The bin width was chosen to be 1 MeV. OPAL tracks the particles in time and dumps the phase space coordinates of every particle after customer specified number of iterations. The figures 6, 7, 9 and 10 contain OPAL data from time tracking. It is important to note that time tracking delivers different results than spatial tracking. Whenever it is important to know, how particles behave at a specific position on the z-axis, a monitor must be placed there. For this reason, the sigma distribution and the correlation matrices were recorded with monitors and plotted in figures 19, 24 and 16.

Monitors save the phase space coordinates of each particle, when they pass the monitors position. In contrast, looking at the bunch distribution in a certain time step, the particle distribution may be expanded over a beam specific length. Estimating beam characteristics for such a distribution is useless, whenever the interest is put on the beam behaviour at a certain place. The beam distribution could smear out certain specifics or falsify respectively create new beam attributes.

References

[AAC+13] Andreas Adelmann, Achim Gsell, Christof Kraus, Yves Ineichen, Steve Russell, Yuanjie Bi, Chuan Wang, Jianjun Yang, Hao Zha, Suzanne Sheehy, Chris Rogers, and Christopher Mayes. *The OPAL Framework, (Object Oriented Parallel Accelerator Library)*, 1.2.0 edition, April 2013.

[Ade13] Andreas Adelmann. Amas code documentation. `http://amas.web.psi.ch/docs/index.html`, January 2013.

[AoC13] The Accelerators and Beam Physics Group of CERN. Mad - methodical acclerator design. `http://mad.web.cern.ch/mad/`, July 2013.

[BAB+12] J. Beringer, J. F. Arguin, R. M. Barnett, K. Copic, O. Dahl, D. E. Groom, C. J. Lin, J. Lys, H. Murayama, C. G. Wohl, W. M. Yao, P. A. Zyla, C. Amsler, M. Antonelli, D. M. Asner, H. Baer, H. R. Band, T. Basaglia, C. W. Bauer, J. J. Beatty, V. I. Belousov, E. Bergren, G. Bernardi, W. Bertl, S. Bethke, H. Bichsel, O. Biebel, E. Blucher, S. Blusk, G. Brooijmans, O. Buchmueller, R. N. Cahn, M. Carena, A. Ceccucci, D. Chakraborty, M. C. Chen, R. S. Chivukula, G. Cowan, G. D'Ambrosio, T. Damour, D. de Florian, A. de Gouvêa, T. DeGrand, P. de Jong, G. Dissertori, B. Dobrescu, M. Doser, M. Drees, D. A. Edwards, S. Eidelman, J. Erler, V. V. Ezhela, W. Fetscher, B. D. Fields, B. Foster, T. K. Gaisser, L. Garren, H. J. Gerber, G. Gerbier, T. Gherghetta, S. Golwala, M. Goodman, C. Grab, A. V. Gritsan, J. F. Grivaz, M. Grünewald, A. Gurtu, T. Gutsche, H. E. Haber, K. Hagiwara, C. Hagmann, C. Hanhart, S. Hashimoto, K. G. Hayes, M. Heffner, B. Heltsley, J. J. Hernández-Rey, K. Hikasa, A. Höcker, J. Holder, A. Holtkamp, J. Huston, J. D. Jackson, K. F. Johnson, T. Junk, D. Karlen, D. Kirkby, S. R. Klein, E. Klempt, R. V. Kowalewski, F. Krauss, M. Kreps, B. Krusche, Yu. V. Kuyanov, Y. Kwon, O. Lahav, J. Laiho, P. Langacker, A. Liddle, Z. Ligeti, T. M. Liss, L. Littenberg, K. S. Lugovsky, S. B. Lugovsky, T. Mannel, A. V. Manohar, W. J. Marciano, A. D. Martin, A. Masoni, J. Matthews, D. Milstead, R. Miquel, K. Mönig, F. Moortgat, K. Nakamura, M. Narain, P. Nason, S. Navas, M. Neubert, P. Nevski, Y. Nir, K. A. Olive, L. Pape, J. Parsons, C. Patrignani, J. A. Peacock, S. T. Petcov, A. Piepke, A. Pomarol, G. Punzi, A. Quadt, S. Raby, G. Raffelt, B. N. Ratcliff, P. Richardson, S. Roesler, S. Rolli, A. Romaniouk, L. J. Rosenberg, J. L. Rosner, C. T. Sachrajda, Y. Sakai, G. P. Salam, S. Sarkar, F. Sauli, O. Schneider, K. Scholberg, D. Scott, W. G. Seligman, M. H. Shaevitz, S. R. Sharpe, M. Silari, T. Sjöstrand, P. Skands, J. G. Smith, G. F. Smoot, S. Spanier, H. Spieler, A. Stahl, T. Stanev, S. L. Stone, T. Sumiyoshi, M. J. Syphers, F. Takahashi, M. Tanabashi, J. Terning, M. Titov, N. P. Tkachenko, N. A. Törnqvist, D. Tovey, G. Valencia, K. van Bibber, G. Venanzoni, M. G. Vincter, P. Vogel, A. Vogt, W. Walkowiak, C. W. Walter, D. R. Ward, T. Watari, G. Weiglein, E. J. Weinberg, L. R. Wiencke, L. Wolfenstein, J. Womersley, C. L. Woody, R. L. Workman, A. Yamamoto, G. P. Zeller, O. V. Zenin, J. Zhang, R. Y. Zhu, G. Harper, V. S. Lugovsky, and P. Schaffner. Review of particle physics. *Phys. Rev. D*, 86:010001, Jul 2012.

[Bau13] Christian Baumgarten. Concerning a double degrader. internal report, PSI, February 2013.

[FAR03] Francis FARLEY. Energy degrader for particle beams. Patent Application, 08 2003. WO 2003/065382 A1.

[Far05] Francis J.M. Farley. Optimum strategy for energy degraders and ionization cooling. *Nuclear Instruments and Methods in Physics Research Section A: Accelerators, Spectrometers, Detectors and Associated Equipment*, 540(2–3):235 – 244, 2005.

[FFR+11] A. Fassò, A. Ferrari, J. Ranft, P.R. Sala, G. Battistoni, F. Cerutti, M. Chin, T. Empl, M. V. Garzelli, M. Lantz, A. Mairani, S. Muraro, V. Patera, S. Roesler, G. Smirnov, F. Sommerer, and V. Vlachoudis. Fluka. `http://www.fluka.org/fluka.php?id=manuals`, 2011.

[Flo03] Klaus Floettmann. Some basic features of the beam emittance. *Phys. Rev. ST Accel. Beams*, 6:034202, Mar 2003.

[GAA+00] D.E. Groom, M. Aguilar-Benitez, C. Amsler, R.M. Barnett, P.R. Burchat, C.D. Carone, C. Caso, G. Conforto, O. Dahl, M. Doser, S. Eidelman, J.L. Feng, L. Gibbons, M. Goodman, C. Grab, A. Gurtu, K. Hagiwara, K.G. Hayes, J.J. Hernández, K. Hikasa, K. Honscheid, C. Kolda, M.L. Mangano, A.V. Manohar, A. Masoni, K. Mönig, H. Murayama, K. Nakamura, S. Navas, K.A. Olive, L. Pape, A. Piepke, M. Roos, M. Tanabashi, N.A. Törnqvist, T.G. Trippe, P. Vogel, C.G. Wohl, R.L. Workman, W.-M. Yao, B. Armstrong, J.L. Casas Serradilla, B.B. Filimonov, P.S. Gee, S.B. Lugovsky, F. Nicholson, K.S. Babu, D. Besson, O. Biebel, P. Bloch, R.N. Cahn, A. Cattai, R.S. Chivukula, R.D. Cousins, T. Damour, K. Desler, R.J. Donahue, D.A. Edwards, J. Erler, V.V. Ezhela, A. Fassò, W. Fetscher, D. Froidevaux, M. Fukugita, T.K. Gaisser, L. Garren, S. Geer, H.-J. Gerber, F.J. Gilman, H.E. Haber, C. Hagmann, I. Hinchliffe, C.J. Hogan, G. Höhler, P. Igo-Kemenes, J.D. Jackson, K.F. Johnson, D. Karlen, B. Kayser, S.R. Klein, K. Kleinknecht, I.G. Knowles, E.W. Kolb, P. Kreitz, R. Landua, P. Langacker, L. Littenberg, D.M. Manley, J. March-Russell, T. Nakada, H.R. Quinn, G. Raffelt, B. Renk, L. Rolandi, M.T. Ronan, L.J. Rosenberg, H.F.W. Sadrozinski, A.I. Sanda, M. Schmitt, O. Schneider, D. Scott, W.G. Seligman, M.H. Shaevitz, T. Sjöstrand, G.F. Smoot, S. Spanier, H. Spieler, M. Srednicki, A. Stahl, T. Stanev, M. Suzuki, N.P. Tkachenko, M.S. Turner, G. Valencia, K. van Bibber, R. Voss, D. Ward, L. Wolfenstein, and J. Womersley. Review of particle physics. *The European Physical Journal*, C15:1+, 2000.

[Jac06] John Davis Jackson. *Klassische Elektrodynamik*. Walter de Gruyter, fourth edition, June 2006.

[LD91] Gerald R. Lynch and Orin I. Dahl. Approximations to multiple coulomb scattering. *Nuclear Instruments and Methods in Physics Research Section B: Beam Interactions with Materials and Atoms*, 58(1):6 – 10, 1991.

[Leo94] William R. Leo. *Techniques for Nuclear and Particle Physics Experiments*. Springer Verlag Berlin Heidelberg GmbH, second edition, 1994.

[Ped12a] Eros Pedroni. Can we improve degrader efficiency? internal presentation, PSI, May 2012.

[Ped12b] Eros Pedroni. Can we improve the performance of a cyclotron beam degradation system by using multiple degraders? internal report, PSI, August 2012.

[Ros52] Bruno Rossi. *High-Energy Particles*. Prentice Hall Incorporated, June 1952.

[SS49] H. S. Snyder and W. T. Scott. Multiple scattering of fast charged particles. *Phys. Rev.*, 76:220–225, Jul 1949.

[Tea] The Root Team. Root - an object oriented data analysis framework. Proceedings AIHENP'96 Workshop, Lausanne, Sep. 1996, Nucl. Inst. and Meth. in Phys. Res. A 389 (1997) 81-86. See also `http://root.cern.ch/`.

[WBM+09] Werner Durandi, Baoswan Dzung Wong, Markus Kriener, Hansruedi Künsch, Alfred Volgelsanger, Samuel Byland, Klemens Koch, Andreas Bartlome, Michael Bleichenbacher, Hans Roth, and Werner Durandi. *Begriffe, Formeln, Tafeln*. Orelli Füssli Verlag AG, Zürich, 2009.

[Zie13] James F. Ziegler. Transport of ions in matter (trim). http://www.srim.org/, May 2013.